FINAL TECHNICAL REPORT

to the

NATIONAL AERONAUTICS AND SPACE ADMINISTRATION
NEPTUNE DATA ANALYSIS PROGRAM

for

"INVESTIGATION OF ATMOSPHERIC WAVES ON NEPTUNE"

GRANT NAGW-2442
SPO Number 8729

for the period
1 March 1991 through 31 August 1994

submitted by

Von R. Eshleman, Principal Investigator
Professor of Electrical Engineering
Durand Building, Room 221
(415) 723-3531

and

David P. Hinson, Co-Investigator
Senior Research Scientist
Durand Building, Room 219
(415) 723-3534

of the

Center for Radar Astronomy
Stanford University
Stanford, CA 94305-4055

SUMMARY

This document constitutes the final technical report for grant NAGW-2442 of the Neptune Data Analysis Program, which supported research concerning atmospheric dynamics on Neptune. Professor Von R. Eshleman was the principal investigator. David P. Hinson was a Co-Investigator. The grant covered the period 1 March 1991 through 31 August 1994, including a six month no-cost extension.

Funding from this grant resulted in publication of one journal article and one book chapter as well as presentation of results at two conferences and in numerous seminars. A complete bibliography is given below. A copy of the journal article is attached along with abstracts from the book chapter and the conference presentations.

With support from this grant we extended our analysis and interpretation of the Voyager 2 radio occultation data beyond what could be accomplished with funding from the Voyager Project. This research contributed to an improvement in our basic understanding of atmospheric dynamics on Neptune. The highlight was the discovery and characterization of inertio-gravity waves in the troposphere and stratosphere. Results include measures of basic wave properties, such as amplitudes and vertical wavelengths, as well as estimates of the effect of the waves on the photochemistry and momentum balance of the upper stratosphere.

This investigation also yielded a better understanding of the potential of radio occultation experiments for studies of atmospheric waves. At the same time we developed new methods of data analysis for exploiting these capabilities. These are currently being applied to radio occultation data obtained with the Magellan spacecraft to study waves in the atmosphere of Venus. Future planetary missions, such as Mars Global Surveyor and Cassini, will benefit from these accomplishments.

BIBLIOGRAPHY

Publications:

Hinson, D. P., and J. A. Magalhães 1993. Inertio-gravity waves in the atmosphere of Neptune. *Icarus* **105**, 142-161.

Ingersoll, A. P., C. D. Barnet, R. F. Beebe, F. M. Flasar, D. P. Hinson, S. S. Limaye, L. A. Sromovsky, and V. E. Suomi 1995. Dynamic meteorology of Neptune. In *Neptune* (D. Cruikshank, Ed.), in press. Univ. of Arizona Press, Tucson.

Abstracts and Conference Presentations:

Hinson, D. P., and J. A. Magalhães. A wave observed in the atmosphere of Neptune. Presented at the 23rd Annual meeting of the AAS Division for Planetary Sciences, 4-8 November 1991, Palo Alto, California. Abstract published in *Bull. American Astronom. Soc.*, vol. 23, no. 3, p. 1164, 1991.

Hinson, D. P. An inertia-gravity wave observed in the atmosphere of Neptune. Presented at the Space Science Series Conference on Neptune and Triton in Tucson, Arizona, 6-10 January 1992 (hosted by the University of Arizona).

Abstract of chapter published in Neptune (D. Cruikshank, Ed.). Univ. of Arizona Press, Tucson.

DYNAMIC METEOROLOGY OF NEPTUNE

ANDREW P. INGERSOLL
California Institute of Technology

CHRISTOPHER D. BARNET
Institute for Space and Terrestrial Science

RETA F. BEEBE
New Mexico State University

F. MICHAEL FLASAR
NASA Goddard Space Flight Center

DAVID P. HINSON
Stanford University

and

SANJAY S. LIMAYE, LAWRENCE A. SROMOVSKY
AND VERNER E. SUOMI
University of Wisconsin

Although Earth-based observations provide hints of Neptune's dynamic activity, most of the observations of cloud patterns, winds, and horizontal variations in temperature are from Voyager. The wind speed varies from 400 m s^{-1} westward at the equator to 250 m s^{-1} eastward at $-70°$ latitude. As on all the giant planets, the winds decay with height in the stratosphere. The meridional contrasts in temperature are small in the upper troposphere and lower stratosphere, with mid-latitude minima that are strangely reminiscent of those on Uranus. The oscillations and motions of Neptune's large spots are more regular than those of Jupiter and Saturn. During the Voyager observations, the Great Dark Spot moved steadily equatorward while it

oscillated in shape with an 8-day period. The latitude and longitude of Dark Spot 2 oscillated with a 36-day period. The small elements within each major feature appeared and disappeared in less than a day. Such activity is remarkable for a planet whose emitted power per unit area is 1/20 that of Jupiter and 1/400 that of the Earth. Weak viscosity can account for the decay of winds in the stratosphere and models without viscosity can account for the spot oscillations. But the wind velocities and temperatures vs. latitude—especially the differences among the giant planets—have not been explained. Major unknowns concern convection and latent heat release, the interaction with Neptune's fluid interior, and the importance of internal energy relative to solar energy in driving the circulation.

I. INTRODUCTION

Planetary atmospheres exhibit a wide range of dynamical phenomena that could not have been predicted from models based on observations of Earth alone. Studying the planets teaches humility. We learn how inventive nature is and how limited our understanding is. Such humility can be useful as we attempt to apply our models to climate states that have never occurred before on Earth, but could occur as we change the composition of the atmosphere and the character of the surface. From the geologic record we know that the Earth's climate has changed drastically—well beyond the limits seen in historical times. Planets provide even more drastic examples of different climates. The insights gained by considering weather and climate processes in exaggerated form on other planets can help us understand such processes on Earth.

In its grand tour of the outer solar system, *Voyager* provided many surprises and several insights into the dynamics of planetary atmospheres. Although the long-lived storms and multiple jet streams of Jupiter had been observed for over 300 years, *Voyager* revealed chaotic small-scale activity that made the large stable structures even more interesting. We learned something about the stability of rotating fluid masses—vortices, and about the persistence of weather patterns in general. When *Voyager* determined the rotation rate of Saturn's interior, it became clear that Saturn's winds approach 500 m s^{-1}—three times greater than Jupiter's, despite the fact that Saturn has less power to drive the winds. *Voyager* images of Uranus showed that the cloud bands are oriented parallel to latitude circles, as they are on the other giant planets, even though the Sun was almost directly overhead at the south pole at the time of the *Voyager* encounter. In these cases we learned

Presented at the 23rd Annual meeting of the AAS Division for Planetary Sciences, 4-8 November 1991, Palo Alto, California. Abstract published in *Bull. American Astronom. Soc.*, vol. 23, no. 3, p. 1164, 1991.

09.04

A Wave Observed in the Atmosphere of Neptune

D. P. Hinson (Stanford) and J. A. Magalhães (NASA/ARC)

We have identified a wave in the atmosphere of Neptune through analysis of radio occultation data from Voyager 2. We employed the following procedure. First, we obtained a vertical profile of number density (n), pressure (p), and temperature (T) vs. radius through Abel inversion of the data. The profile spans pressures from a few tenths of a mb to more than 1 bar. Second, we separated structure on different spatial scales by filtering the profile. Low-pass output from the filter gives the quiescent background structure of the atmosphere at a resolution of 20 km, comparable to a pressure scale height. High-pass output from the filter isolates the perturbations in temperature (δT) and number density (δn) relative to this background structure on spatial scales less than 20 km. The profiles of δT and δn have a diffraction-limited vertical resolution of 1–2 km. Next, we applied a simple, linear theory for atmospheric waves to model the behavior expected for a wave propagating through the observed background structure of Neptune's atmosphere. Agreement between predictions of the theory and observations of δT and δn vs. p gives strong evidence for the presence of a wave at 44°S lat (planetocentric). The wave appears to propagate with little or no attenuation at pressures between 3 and 100 mb. Observations at lower pressures are hampered by noise limitations of the data; however, we hope to extend the observations to greater pressures with further analysis. Preliminary results include a vertical wavelength of about 1/3 to 1/2 of a pressure scale height and an amplitude of about 0.2 K at 80 mb, increasing to about 1 K at 6 mb. Theory and observations suggest that the wave begins to break at a pressure near 1 mb, leading to eddy mixing of the atmosphere at lower pressures. Other basic properties of the wave, including its classification (e.g., Rossby, inertia-gravity, ...), remain uncertain at present. Preliminary results for Neptune will be compared with analogous results derived previously for Uranus (Hinson and Magalhães 1991, Equatorial waves in the stratosphere of Uranus, *Icarus*, in press).

This work is funded under NASA grant NAGW-2442 (NDAP).

Presented at the Space Science Series Conference on Neptune and Triton in Tucson, Arizona, 6-10 January 1992 (hosted by the University of Arizona).

An Inertia-Gravity Wave Observed in the Atmosphere of Neptune

David P. Hinson
Center for Radar Astronomy
Stanford University

Atmospheric waves on Neptune can be identified and studied through use of radio occultation data from Voyager 2. The analysis and interpretation of the data proceeds as follows. First, I obtained a vertical profile of number density (n), pressure (p), and temperature (T) vs. radius through Abel inversion of the data. The profile spans pressures from a few tenths of a mb to more than 1 bar. Second, I separated structure on different spatial scales by filtering the profile. Low-pass output from the filter gives the quiescent background structure of the atmosphere at a resolution of 15 km, comparable to a pressure scale height. For studies of atmospheric waves, the key parameter characterizing the background structure is the buoyancy (or Brunt-Väisälä) frequency (N) which I computed directly from the filtered temperature profile. High-pass output from the filter isolates the perturbations in temperature (δT) and number density (δn) relative to this background structure on spatial scales less than 15 km. The profiles of δT and δn have a diffraction-limited vertical resolution of about 1 km.

I applied a linear theory for atmospheric waves to model the behavior expected for a wave propagating through the background structure observed on Neptune. The theory includes the effect of weak vertical wind shear and yields a WKB solution for the wave's vertical structure (cf. Lindzen 1981, *J. Geophys. Res.* **86**, 9707–9714). A central feature of this solution is that both wind shear and vertical variations in N can cause the wave amplitude and vertical wavelength to vary distinctively with height. Agreement between predictions of the theory and observations of δT and δn vs. p gives strong evidence for the presence of an inertia-gravity wave at 44°S (planetocentric), 230°W (NLS). [A Rossby-wave interpretation of the data encounters serious problems arising from the implied extremely low frequency of the wave (cf. French and Gierasch 1974, *J. Atmos. Sci.* **31**, 1707–1712).] The wave appears to propagate with little or no attenuation at pressures between 3 and 100 mb. Observations are hampered by noise limitations at lower pressures but should be possible at greater pressures with further analysis. Results to date include a vertical wavelength of about 8 km and an amplitude of 0.2 K at 80 mb, increasing to 1 K at 6 mb. Predictions of the theory show improved agreement with the data when a uniform vertical wind shear is included in the theoretical model. When combined with the value for wind shear at this latitude inferred from Voyager IRIS observations (Conrath *et al.* 1991, *J. Geophys. Res.*, in press), this result provides an important constraint on the zonal phase speed — a wave property which cannot otherwise be inferred from these observations. In future work, I hope to estimate the momentum flux carried by the wave, the breaking level, and the eddy mixing and acceleration of the mean winds that accompany wave dissipation (cf. Hinson and Magalhães 1991, *Icarus*, in press).

This work is funded under NASA grant NAGW-2442 (NDAP).

ICARUS 105, 142–161 (1993)

Inertio-Gravity Waves in the Atmosphere of Neptune

DAVID P. HINSON

Center for Radar Astronomy, Stanford University, Stanford, California 94305-4055

AND

JULIO A. MAGALHÃES

NASA Ames Research Center, Moffett Field, California 94035

Received January 19, 1993; revised May 21, 1993

A refined analysis of Voyager 2 radio occultation data has revealed distinct, quasi-periodic temperature variations in the troposphere and stratosphere of Neptune. Temperature oscillations with amplitudes of 0.1–1 K and vertical wavelengths of 1–10 km are present at latitudes 61°N (ingress) and 45°S (egress). We used techniques of spectral analysis to identify the predominant periodicities of the data and applied digital filters to isolate signal perturbations within selected wavelength passbands. Basic results include detailed vertical profiles of the temperature perturbations associated with these atmospheric waves. The data also provide a weak constraint on the horizontal structure—the horizontal wavelength probably exceeds the vertical wavelength by at least an order of magnitude. We confined our interpretation to two waves in the stratosphere whose vertical structure was characterized over 9 and 15 cycles of oscillation, respectively, spanning 2 to 3 pressure scale heights. In both cases, the observations are consistent with the characteristics of inertio-gravity waves, but cannot be reconciled with a Rossby-wave interpretation. We applied standard theory to model the wave behavior and to estimate the wave contributions to the eddy mixing and momentum budget of the middle atmosphere. The exponential growth of wave amplitude with height should result in overturning, or wave breaking, at pressures less than about 0.5 mbars for one wave and about 3 mbars for the other. The process of wave dissipation, though poorly understood, may be a significant source of "eddy mixing" on Neptune, with wave-generated eddy diffusivities as large as 50 m^2 sec^{-1}. The wave forcing of the mean flow that accompanies dissipation could alter the zonal winds by as much as about 9 m sec^{-1} per planet rotation.

INTRODUCTION

The Voyager 2 spacecraft completed its "grand tour" of the outer Solar System with a close flyby of Neptune in August 1989 (Stone and Miner 1989). The sequence of near encounter observations included a radio occultation experiment for remote sensing of Neptune's atmosphere at mid-latitudes in both hemispheres. Results already derived from the data include (Lindal 1992): a temperature profile spanning pressures from 0.35 to 6300 mbars; a helium abundance (from comparison with Voyager IRIS data) of 19 ± 3% by volume; detection of a thin methane cloud layer near the 1800-mbar pressure level; an inferred methane mixing ratio of about 2% below the condensation level; detection of substantial signal attenuation in the deeper troposphere, which was attributed to absorption by ammonia vapor; an ammonia mixing ratio of 500 ± 150 parts per billion at the level where the pressure and temperature are 6300 mbars and 135 K, respectively; and an inferred prograde zonal wind speed of 176 ± 32 m sec^{-1} in the troposphere at 60°N latitude.

Against this background, we have used the Voyager 2 radio occultation data to conduct a complementary investigation of atmospheric waves in the troposphere and stratosphere of Neptune. We extracted our principal results from the basic measurements through use of the standard, "Abel transform" algorithm for reduction of radio occultation data, supplemented by digital filters specialized to the study of atmospheric waves. This approach to data analysis represents an extension of techniques developed and applied originally by Hinson and Magalhães (1991) in a similar study of atmospheric waves on Uranus.

We restricted our attention to the stratosphere and upper troposphere, where the atmosphere is stably stratified. We also limited the investigation to atmospheric structure on spatial scales exceeding the Fresnel scale, F, which is about 1 km for the Neptune occultation geometry. This second condition is convenient for two reasons (cf. Hinson and Magalhães 1991). First, diffraction effects are negligible for atmospheric structure on scales exceeding

0019-1035/93 $5.00

F by a factor of 2–3. The propagation of electromagnetic waves through such structure can therefore be modeled accurately through use of geometrical optics, which simplifies the analysis considerably. Second, frequency (or phase) data are far more sensitive than amplitude data to atmospheric structure over these spatial scales. Accordingly, we based our investigation entirely on frequency measurements, which led to a more compact presentation of the basic results.

Conrath *et al.* (1991a) have identified a planetary-scale wave on Neptune in the latitude band between 10°S and 30°S through analysis of infrared spectra obtained in a global mapping sequence with the Voyager IRIS instrument. The vertical scale of the wave is most likely comparable to or greater than one pressure scale height (~20 km), the vertical resolution of the instrument. We show here through analysis of Voyager radio occultation data that the atmosphere of Neptune also exhibits distinct, quasi-periodic spatial variations in temperature on vertical scales of about 1–10 km. Structure on these scales is present at both occultation ingress (61°N) and occultation egress (45°S). However, due to differences in their locations and vertical wavelengths, the wave features observed by these two instruments are probably not related. (See Ingersoll *et al.* [1993] for a comprehensive review of atmospheric dynamics, including waves, on Neptune.)

One aspect of our results deserves emphasis. The amplitude in temperature of an atmospheric wave generally increases exponentially with height, but this growth in wave amplitude is eventually limited by convective instability. In Neptune's stratosphere, the maximum amplitude is less than 2 K when the vertical wavelength is 5 km. Our ability to identify and accurately characterize such waves illustrates the sensitivity and vertical resolution of the radio occultation technique.

Apart from their intrinsic interest, atmospheric waves deserve study for several reasons. It is well known from terrestrial research that waves can have a substantial impact on the momentum budget and thermal structure of the middle atmosphere (i.e., the region bounded by the tropopause and homopause). Estimates of the wave forcing of the mean flow that accompanies dissipation can thus contribute to a better understanding of the dynamical state of the atmosphere. Atmospheric waves also respond sensitively to wind shear and to changes in the background stratification so that observations of propagating waves can in principle reveal characteristics of the basic atmospheric structure and circulation (cf. Flasar and Gierasch 1986). Moreover, the implications of wave studies go beyond the subject of atmospheric dynamics. By generating eddy mixing during dissipation, waves can enhance the transport of trace constituents and thereby influence the photochemistry of the upper atmosphere. This investigation is motivated by an interest in these diverse aspects of wave behavior.

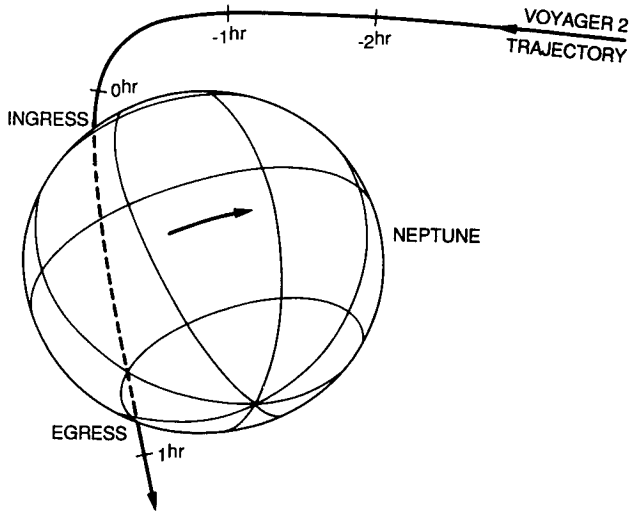

FIG. 1. Schematic view from Earth of Neptune and the trajectory of Voyager 2 (from Lindal 1992). The spacecraft position is marked at 1-hr intervals relative to the time at closest approach to Neptune. Radio occultation measurements of the neutral atmosphere began near 61°N latitude and ended near 45°S. The distance from the spacecraft to the center of Neptune increased during the occultation from about 30,500 km at ingress to about 76,900 km at egress. The distance from spacecraft to Earth was about 4.43×10^9 km.

OBSERVATIONS AND DATA ANALYSIS

This section begins with a discussion of the experiment geometry, the relevant spacecraft and ground equipment, and the initial steps of data processing. We then describe the procedure used to extract results of interest from the basic measurements. We include a discussion of the standard algorithm for reduction of radio occultation data—the Abel transform—which is based on the laws of geometrical optics. However, as the mathematical foundation for this algorithm is well established (Fjeldbo and Eshleman 1968, Fjeldbo *et al.* 1971, Eshleman 1973, Tyler 1987), we limit the discussion to general concepts and parameter definitions. We then introduce a type of digital filter that is central to this investigation.

Figure 1 shows the view from Earth of Voyager 2 as it passed behind Neptune. Subsequent sections give a more detailed description of the experiment geometry.

The Voyager 2 spacecraft carries a temperature-controlled "ultrastable" quartz oscillator (USO) designed to provide a steady reference signal for use in radio occultation experiments (Eshleman *et al.* 1977). During the occultation by Neptune, the spacecraft employed the USO in generating a pair of signals at coherently related frequencies of 2296 and 8420 MHz (wavelengths of 13.1 and 3.6

cm) with an exact frequency ratio of 3 : 11. These signals are commonly referred to as *s*-band and *x*-band, respectively. Both signals were amplified and transmitted continuously without modulation in right-circular polarization through the 3.7-m-diameter spacecraft antenna. The performance of the USO and other spacecraft radio equipment is such that stochastic variations in the frequency of the radiated signals do not exceed a few parts in 10^{12} over the time scales of interest here (about 1–100 sec).

The signals transmitted by Voyager 2 during the Neptune occultation were received by three independent ground antennas (Tyler *et al.* 1989): the 70-m-diameter antenna of the NASA Canberra Deep Space Communications Complex (Australia), which recorded data at both wavelengths; the 64-m antenna of the Parkes Radio Astronomy Observatory (Australia), which recorded data only at 3.6 cm; and the 64-m antenna of the Institute of Space and Astronautical Science (Japan), which recorded data only at 13.1 cm. As the Camberra tracking station yielded data with a higher signal-to-noise ratio (SNR) at both wavelengths than its counterparts, only the data from Canberra are considered here.

The radio signals received at Canberra were amplified, filtered, heterodyned (mixed) to baseband, digitized to 8-bit samples, and recorded on computer tapes at sampling rates of 50,000 sec^{-1}. All receiving equipment was designed to operate without degrading the inherent frequency stability of the signals radiated by Voyager 2. This combination of spacecraft and ground equipment yielded preingress and postegress SNRs in a 1-Hz bandwidth of about 900 (29.5 dB) and 33,000 (45.2 dB) at wavelengths of 13.1 and 3.6 cm, respectively.

After receiving copies of the data tapes from Canberra, we applied standard techniques of digital signal processing to measure signal parameters of interest (cf. Bracewell 1986, Oppenheim and Schafer 1975, Brigham 1974). First, we used a bandpass filter to remove a substantial amount of thermal noise from the data. This step reduced the sampling rate by a factor of 16 while preserving all useful information contained in the radio signals from Voyager 2. We then obtained time histories of signal frequency, $f(t_i)$, through spectral analysis (Lipa and Tyler 1979). (The integer index i is included as a reminder that data are sampled discretely.) We computed results at sampling rates of 24.41, 12.21, and 6.10 sec^{-1} for the measurements at both wavelengths. This range of sampling rates was chosen to include both higher values, which provide finer spatial resolution, as well as lower values, which reduce fluctuations caused by thermal noise. Unless noted otherwise, all results presented below were obtained from data with a sampling rate of 12.21 sec^{-1}. However, we confirmed the reliability of all results and tested their sensitivity to the effects of thermal noise by using data at the higher and lower sampling rates. These dual-wavelength measurements of f are the basis for our studies of atmospheric waves and the background thermal structure in the troposphere and stratosphere of Neptune.

The full procedure for reducing radio occultation data from an oblate planet like Neptune is described in detail by Lindal (1992). This formalism properly accounts for the distortion of isopycnal surfaces caused by gravitational, centrifugal, and Coriolis forces. While this rigorous approach is essential to obtaining accurate results from the deeper troposphere of Neptune (e.g., for inferring the local zonal wind speed and the abundances of CH_4 and NH_3), we found that a less accurate but much simpler procedure can yield reliable results at pressures of 0.1–1000 mbars, the range of interest here. In this alternate approach, we used a fitted sphere to model the local shape of Neptune near ingress or egress. Model parameters were chosen so as to mimic the effect of oblateness on the radio signals. We then reduced the data by applying the simpler formalism appropriate to a spherical atmosphere, as described below, but using an effective local center of curvature that is displaced from Neptune's center of mass.

We constructed the equivalent spherical models for Neptune's atmosphere in two steps. First, we computed the dynamical shape of a selected isopycnal surface (cf. Lindal *et al.* 1985). This requires a measure of the absolute radius of the surface at a reference latitude (obtained from the radio occultation data) as well as measurements of the gravity field (Anderson *et al.* 1992), Neptune's rotation rate (Warwick *et al.* 1989), and the profile of zonal wind speed as a function of latitude (Limaye and Sromovsky 1991). Second, we used these results for the dynamical shape to calculate the location of the effective center of curvature at the two regions of interest (near 61°N and 45°S) taking into account the experiment geometry.[1] A complication arises in that the location of the center of curvature varies with time during the experiment as a consequence of spacecraft motion, the experiment geometry, and the variation of Neptune's shape with latitude and pressure. However, this motion of the center of curvature was found to have an insignificant effect on the retrieved temperature profiles over the range of pressures considered here. Accordingly, we used a fixed center of curvature in reducing the data at ingress or egress.

The remaining steps of data analysis rely on the assump-

[1] The location of the effective center of curvature depends on: (1) the positions relative to Neptune of the spacecraft and the ground antenna (with appropriate light propagation-time corrections); (2) the orientation of the spin axis; (3) the projected shape of the isopycnal surface as viewed from the spacecraft and the ground antenna (i.e., Neptune's limb); and (4) the curvature of the isopycnal surface in the plane containing the effective center of curvature, the spacecraft, and the ground antenna. For further discussion, see Eshleman (1975), Hubbard *et al.* (1975), Hubbard (1976), and Kliore and Woiceshyn (1976).

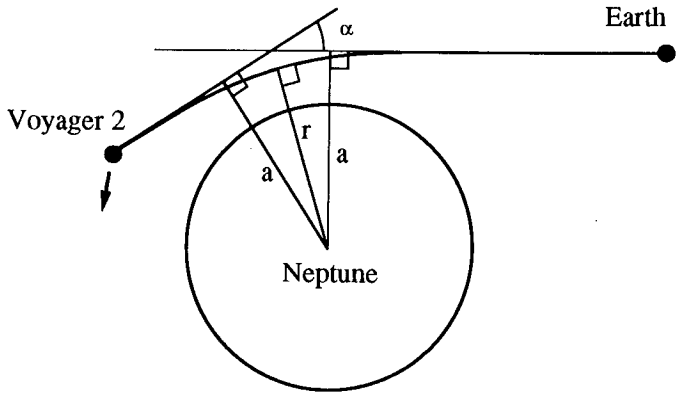

FIG. 2. Idealized representation of the experiment geometry showing the instantaneous ray path followed by radio signals propagating from Voyager 2 to Earth. The local shape of Neptune is modeled using a sphere as explained in the text. Radial gradients of atmospheric refractive index cause the ray path to bend by an angle α, which depends strongly on the impact parameter a. For reference, α was about 0.038 radians (2.2°) for the ray path that grazed the 1000-mbar pressure level at egress.

tion that the refractive index of the atmosphere, μ, depends only on the radial distance, r, from the local center of curvature. (The validity and implications of this assumption are considered below.) Figure 2 shows a schematic of the occultation geometry and introduces key parameters. Within the framework of geometrical optics, the radio signals propagating from spacecraft to Earth follow a distinct trajectory, or ray path, which corresponds to a stationary value of the path integral of refractive index (Born and Wolf 1975). The ray trajectory is a straight line in a vacuum but curves within the atmosphere of Neptune in response to gradients in μ. The net refractive bending angle, α, is a strong function of the impact parameter, a, defined as the distance from Neptune's local center of curvature to the straight line followed by the ray approaching (or receding from) the atmosphere. The assumption that μ depends only on r has two notable consequences. First, the ray path always remains in the plane containing the spacecraft, the ground station, and Neptune's local center of curvature. Second, $\mu(r)$ can be obtained uniquely from $\alpha(a)$ through an Abel transform. [See Bracewell (1986, p. 262) for a discussion of the Abel transform and its properties.]

The frequency, $f(t_i)$, of a signal received at the ground antenna depends, among other things, on the Doppler shift caused by motion of the spacecraft, which in turn depends strongly on α. We exploited this relationship to obtain $\alpha(a_i)$ from $f(t_i)$ using the reconstruction of the spacecraft trajectory provided by the Voyager Navigation Team. This step is straightforward, requiring only basic laws of geometrical optics and a relativistic formula for the Doppler shift. We then obtained $\mu(r_i)$ from $\alpha(a_i)$ through numerical integration.

Other atmospheric parameters can be derived from the refractive index profile. Analysis of Voyager observations suggests that H_2 and He are the principal constituents of the stratosphere and upper troposphere with the relative abundances given in Table I (Conrath *et al.* 1991b). (Minor constituents, such as CH_4, have a negligible effect on the net refractive index of the atmosphere at pressures 0.1–1000 mbars, so they are ignored here.) We converted $\mu(r_i)$ to a vertical profile of mass density, $\rho(r_i)$, for this observed composition using laboratory data on the microwave properties of H_2 and He (e.g., Orcutt and Cole 1967, Lindal *et al.* 1987). Next, we assumed that the atmosphere is in hydrostatic equilibrium in the vertical direction, so that the pressure at a given radius, $p(r_i)$, matches the weight of the overlying column of gas, which we calculated from $\rho(r_i)$ using the measurements of the gravity field and rotation rate mentioned earlier. Finally, we obtained a temperature profile, $T(r_i)$, by using these results for $\rho(r_i)$ and $p(r_i)$ along with the ideal gas law.

This procedure for data reduction also yields parameters that characterize the geometry of the ray path and its variation with time. These include the latitude and longitude at the point of closest approach to Neptune, which we will refer to as the proximate point on the ray path. The solution for the motion of the proximate point (latitude and longitude vs pressure) provides a useful characterization of the experiment geometry (see Fig. 13, below). We also used these results to relate the basic measurements, $f(t_i)$, to the pressure, p_i, and radius, r_i, of the proximate point, which proved useful in analyzing the data and interpreting the results.

Having described the general procedure for reducing radio occultation data, we now consider its application to studies of atmospheric waves. The radio occultation measurements pertaining to pressures between 0.1 and 1000 mbars were obtained in a short interval (about 100 sec at ingress and 230 sec at egress) as the ray path sliced rapidly through Neptune's atmosphere. Because these

TABLE I
Composition and Thermodynamic Properties of the Upper Troposphere and Stratosphere

Parameter	Value
Mole fraction of H_2	81%
Mole fraction of He	19%
Gas constant, R	3500 m^2 sec^{-2} K^{-1}
Specific heat at constant pressure,[a] c_p	9100 m^2 sec^{-2} K^{-1}

[a] Assuming "frozen equilibrium" hydrogen at 80 K.

time spans are much shorter than the period of any atmospheric waves expected to be present on Neptune (see below), the retrieved temperature profiles give a snapshot of the instantaneous atmospheric structure at ingress and egress. An investigation of atmospheric waves is possible with this type of data provided that any wave-induced temperature perturbations can be distinguished clearly from the background thermal structure. This can be a difficult task when the vertical scale of the waves is comparable to or larger than a pressure scale height. However, the signature of atmospheric waves with smaller vertical wavelengths can be readily identified through use of an appropriate spatial filter.

We chose for this application a digital filter based on least-squares fitting of quadratic polynomials (Hamming 1989). The filter was applied to the basic frequency data as follows. First, we obtained the radius, r_i, at the proximate point for the data sample of interest, $f(t_i)$, through direct inversion of the occultation measurements. Next, we identified all data samples whose corresponding proximate radii fall within a prescribed altitude interval d centered on r_i. We then fit a quadratic polynomial by least squares to this segment of frequency data using time as the independent variable. The value of the fitted polynomial at t_i, the time of the central data sample, represents one sample of output from a "low-pass" filter. Conversely, the difference between the central data sample and the fitted polynomial at time t_i represents one sample of output from a "high-pass" filter. We repeated this procedure for each discrete sample of frequency.

The operation of the filter can be expressed as

$$f(t_i) = f_0(t_i) + f'(t_i), \tag{1}$$

where f_0 is the value of the fitted polynomial. The filter separates the data into two components, one (f_0) that varies slowly with time, and another (f') that comprises relatively rapid variations about the mean. When used in conjunction with the procedure for data reduction described above, and with the proper choice for the parameter d, this filter is capable of separating the background thermal structure of the atmosphere from the temperature perturbations caused by atmospheric waves. The same type of filter was applied previously by Hinson and Magalhães (1991) in a similar study of atmospheric waves on Uranus.

The properties of this filter can be described through use of a dimensionless transfer function, $B(\lambda)$, defined as the ratio of filter output to input when the latter is a sinusoid of spatial period λ. Figure 3 shows $B(\lambda)$ for both the low-pass and the high-pass filters when d is 20 km. The chief limitation of these filters arises from the ripples that appear when $\lambda < 10$ km. These cause distortion in the output from the high-pass filter while allowing signals with high spatial frequencies to leak (with attenuation) into the output from the low-pass filter. However, this did not appear to be a serious problem in the present application, and we chose this filter over numerous alternatives because of its simplicity.

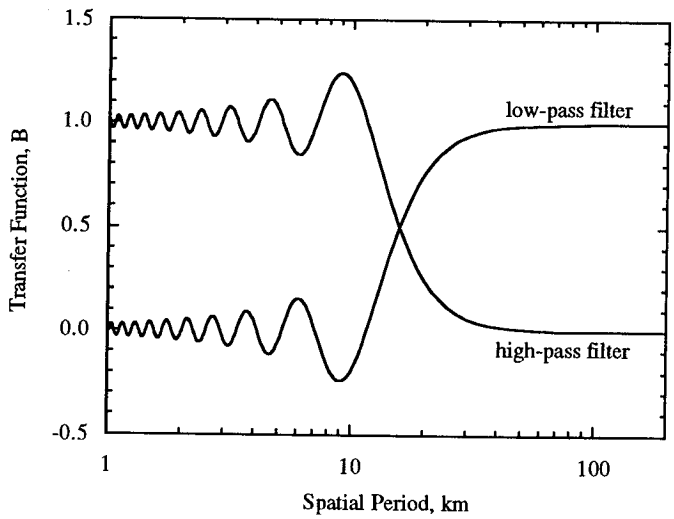

FIG. 3. Characteristics of the spatial filter applied to the radio occultation data. The dimensionless transfer function B gives the ratio of filter output to input when the latter is a sinusoid with spatial period λ. Curves show B for low-pass and high-pass filters when the parameter d = 20 km. The transfer functions for these two filters are equal (B = 0.5) when $\lambda \approx 16$ km, corresponding to the spatial resolution of output from the low-pass filter.

Finally, we note that x-band data have two important advantages over s-band data for remote sensing of Neptune's neutral atmosphere. First, the SNR is higher at x-band by a factor approaching 40 for the data considered here. Second, data at the shorter wavelength are far less affected by Neptune's ionosphere. Quantitatively, the Doppler shift in frequency caused by the neutral atmosphere is 11/3 times larger at x-band than at s-band, whereas the reverse is true for the Doppler shift caused by the ionosphere. Both factors enhance the sensitivity of the x-band data to the small frequency perturbations caused by waves in the neutral atmosphere. Accordingly, all results presented in the next section were derived entirely from measurements at 3.6-cm wavelength.[2]

[2] In a previous study of waves in the neutral atmosphere of Uranus, we used measurements at s-band to remove plasma effects from the x-band data (Hinson and Magalhães 1991). We computed the analogous correction term for the Neptune occultation data but found it to be negligible, at least for the subset of data considered here. Hence, we decided to forgo the plasma correction in order to avoid needlessly contaminating the x-band data with additional thermal noise.

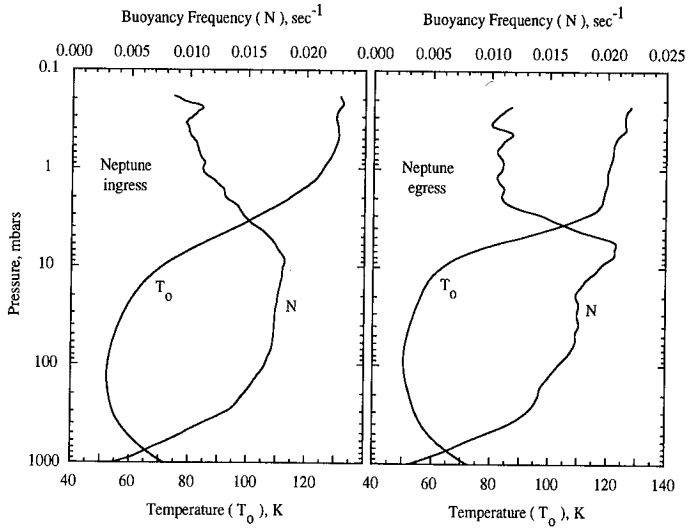

FIG. 4. Vertical profiles of temperature, T_0, and buoyancy frequency, N, obtained from frequency measurements at a sampling rate of 6.10 Hz. Data were smoothed to a vertical resolution of about 16 km before inversion. The resulting profiles characterize the background structure of the stratosphere and upper troposphere.

RESULTS

When applied to the radio occultation data from Neptune, the method of analysis described in the previous section yielded complementary results concerning not only atmospheric waves in the upper troposphere and stratosphere but also the ambient structure through which the waves propagate. The results for the background structure are presented first, followed by a discussion of the waves and their basic characteristics.

Background structure. Figure 4 shows vertical profiles of temperature, T_0, retrieved from the smoothed frequency data, f_0. We used a *low-pass* filter with $d = 20$ km during data reduction, yielding profiles with a vertical resolution of about 16 km (cf. Fig. 3). The tropopause, defined as the temperature minimum that separates the stratosphere from the troposphere, appears at a pressure near 100 mbars, where $T_0 \approx 50$ K. The vertical resolution of the profiles was chosen to match the pressure scale height, $H \equiv RT_0/g$, at the tropopause, where R is the gas constant and g is the acceleration of gravity. Recalling that the low-pass filter suppresses any temperature oscillations on scales smaller than 16 km, and noting that wave-like features with larger vertical scales are not evident in Fig. 4, we take these profiles to be representative of the background structure of Neptune's atmosphere.

The ingress profile in Fig. 4 is slightly warmer than the results tabulated by Lindal (1992). The difference is 1.9 K at a pressure of 1 mbar, decreasing steadily to 0.3 K at 1000 mbars. As the uncertainties in the measurements at these two pressures are about 12 and 2 K, respectively (Lindal 1992), the difference is not statistically significant. This small temperature bias had no appreciable effect on the results reported here.

Figure 4 also shows profiles of the buoyancy (or Brunt–Väisälä) frequency, N, defined as

$$N \equiv \left[\frac{g}{T_0}\left(\frac{\partial T_0}{\partial z} + \frac{g}{c_p}\right)\right]^{1/2}. \quad (2)$$

Here, z is geometric height and c_p is the specific heat at constant pressure. We computed N from the measured temperature profiles using values for g and c_p appropriate to Neptune.

The quantity N is both a natural measure of static stability and a key parameter affecting the behavior of atmospheric waves (Gill 1982, Andrews *et al.* 1987). It is largest in the lower stratosphere (5–10 mbars), where T_0 increases rapidly with height. In the troposphere, N decreases steadily with increasing pressure as $\partial T_0/\partial z$ approaches the dry adiabat, $-g/c_p$. A fluid parcel displaced vertically will tend to oscillate about its equilibrium position with angular frequency N (Turner 1973).

Table II lists relevant characteristics of the background structure of the stratosphere. The results for r_0, T_0, H, and N were obtained as part of this work. Values for other parameters were either taken directly or derived from references already cited.

Wave perturbations to received signal frequency. An atmospheric wave modulates the ambient structure of a planetary atmosphere, producing a periodic pattern of spatial (and temporal) variations in μ, ρ, and T. During

TABLE II
Physical Characteristics of the Stratosphere of Neptune[a]

Parameter	61°N	45°S	Units
Planet radius,[b] r_0	24,530	24,650	km
Coriolis parameter, f	+1.90	−1.53	10^{-4} sec^{-1}
Planetary vorticity gradient, β	4.28	6.22	10^{-12} m^{-1} sec^{-1}
Gravitational acceleration, g	11.2	11.1	m sec^{-2}
Adiabatic lapse rate, g/c_p	1.2	1.2	10^{-3} K m^{-1}
Background temperature, T_0	71	63	K
Pressure scale height, H	22	20	km
Brunt–Väisälä frequency, N	1.8	1.9	10^{-2} sec^{-1}

[a] Value given at 10-mbar pressure level for vertically varying parameters.
[b] Measured from center of mass of Neptune.

an occultation experiment, this atmospheric modulation in turn causes perturbations to the bending angle α and, hence, to f. The characteristics of the frequency fluctuations are determined by the experiment geometry and the spatial structure of the atmospheric wave.

Data from a single radio occultation experiment are not sufficient for reconstructing the full three-dimensional structure of an atmospheric wave. There is an inherent ambiguity in the data that affects measurements of not only the vertical and horizontal wavelengths but also the wave amplitude. The simplest way to avoid this ambiguity is by assuming that the horizontal wavelength (or characteristic scale) of each wave is much larger than its vertical wavelength. The observed, quasi-periodic perturbations in f can then be attributed entirely to wave-induced *vertical* variations in μ. In addition, the wave amplitude can be retrieved reliably through use of the Abel transform. We adopted this assumption in deriving our fundamental results, which appear in Figs. 5–11. We will discuss its implications after the basic results have been presented.

Proceeding with the data analysis, we labeled each data sample with the pressure, p_i, and radius, r_i, of the corresponding proximate point on the ray path. These parameters were obtained as a byproduct of the analysis that led to the profiles in Fig. 4. We then applied a *high-pass* filter with $d = 20$ km to the frequency data yielding the perturbations, f', that result from atmospheric structure on vertical scales smaller than about 16 km. The resulting profiles of f' vs p_i or r_i are the basis of the results shown in Figs. 5–7.

We applied techniques of spectral analysis to characterize these frequency perturbations. Two different approaches were used. In one, we first interpolated the data to obtain samples with uniform spacing in ray altitude for pressures between 1 and 1000 mbars. After applying a Hamming window[3] to the interpolated data, we computed the discrete spatial Fourier transform and its squared magnitude, the power spectrum (Bracewell 1986). In our second approach to spectral analysis, we adopted a least-squares procedure that can be applied directly to unequally spaced data (Lomb 1976, Press and Teukolsky 1988), thus avoiding the need for interpolation. The power spectra calculated by these two methods are in close agreement. Figure 5 shows the results at both ingress and egress.

We used numerical simulations supplemented by standard results from statistical analysis to characterize the effects of thermal noise, the main source of error in the measured spectra. The simulations show that the probability of a random peak exceeding 1 Hz^2 is less than 10^{-3}. (For reference, each measured spectrum contains about 800 discrete samples.) Moreover, as a first approximation, the spectrum resulting from thermal noise should follow a χ^2 distribution with 2 degrees of freedom (Jenkins and Watts 1968).

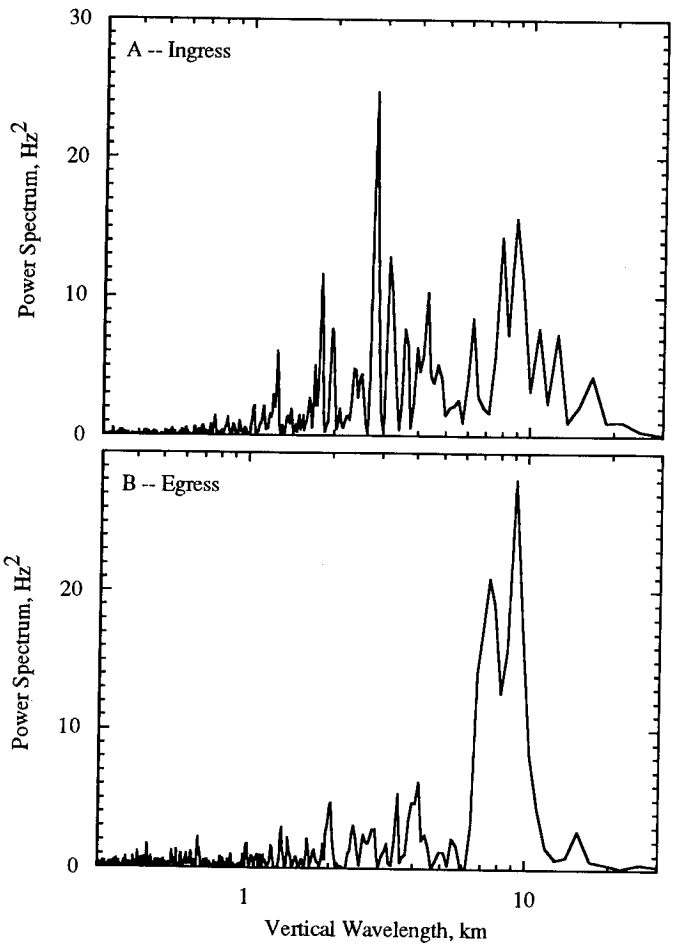

FIG. 5. Power spectra of frequency fluctuations, f', as a function of vertical wavelength. Results at both ingress and egress were obtained from data at pressures 1–1000 mbars. The dominant features in both spectra reflect structure in the atmosphere of Neptune. Random peaks caused by thermal noise should seldom exceed 1 Hz^2.

At ingress (Fig. 5a), the measured spectrum exhibits numerous peaks that are well above the noise level, indicating the presence of atmospheric structure over a range of vertical scales. The most prominent feature is a narrow peak with a periodicity of about 3 km. In contrast, the spectral power at egress (Fig. 5b) is concentrated within spatial scales of about 7–10 km, and structure on smaller vertical scales is more subdued than at ingress.

In order to take a closer look at this atmospheric structure, we separated f' into two components through additional filtering:

[3] Window functions (Harris 1978) are commonly used in spectral analysis to suppress "leakage" effects, which occur when the length of the data interval used in the Fourier transform is not an integer multiple of the periodicity of the data (Brigham 1974).

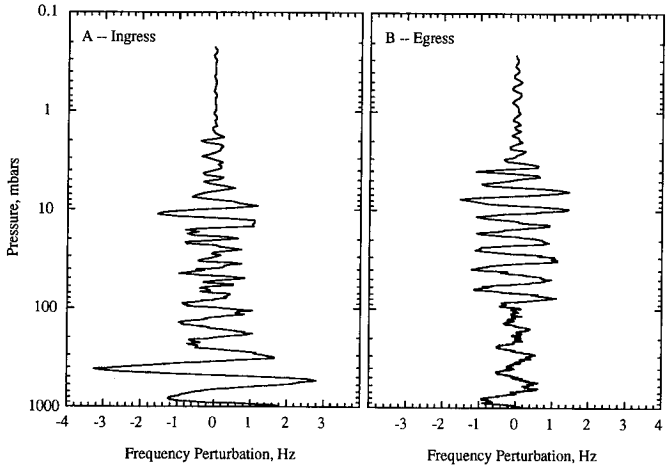

FIG. 6. Frequency perturbations, f_1', that result from atmospheric structure with vertical wavelengths of 4–16 km. Measurements exceed the noise level at pressures greater than 2–3 mbars.

$$f' = f_1' + f_2'. \tag{3}$$

The second term, f_2', is the result of applying a high-pass filter with $d = 5$ km to the original frequency data, while the first term, f_1', is the difference between f' and f_2'. Hence, one component, f_1', is sensitive to atmospheric structure with vertical wavelengths of about 4–16 km, while the other component, f_2', results from vertical structure smaller than about 4 km. This strategy for subdividing f' was guided by the appearance of the measured spectra.

Figure 6 shows f_1' vs p_i at both ingress and egress. The sensitivity of these measurements was limited to about 0.1 Hz, roughly independent of p_i, by thermal noise. Structure in the neutral atmosphere produced frequency perturbations that exceed this noise level for pressures greater than 2–3 mbars at both locations. The most striking aspect of the data is the periodic oscillations that appear at egress at pressures of 3–90 mbars. This feature is responsible for the predominant spectral peak in Fig. 5b. The frequency perturbations at ingress, though generally more irregular in appearance than those at egress, include wave-like oscillations at pressures 80–1000 mbars. As one indication of the sensitivity of the measurements, we note that a 1-Hz variation in f_1', which is easily detectable, corresponds to a change in α of only 3 μrads.

Figure 7 shows analogous measurements of f_2' vs p_i. As in Fig. 6, the noise level at low pressures is about 0.1 Hz, but the impulsive fluctuations caused by thermal noise increase (with decreasing SNR) to about 0.4 Hz at 50 mbars. (This component of thermal noise was largely removed from the data in Fig. 6 by the low-pass filter with $d = 5$ km.) Observations of f_2' at pressures exceeding 50 mbars are strongly affected by thermal noise and will not be considered here. The effect of small-scale structure in the neutral atmosphere is evident at both ingress and egress for pressures greater than 2–3 mbars. Measurements at ingress exhibit strong, quasi-periodic oscillations at pressures of 4–40 mbars. In contrast, signal fluctuations at egress are more subdued and less structured. These characteristics of the data in Fig. 7 are consistent with the appearance of the spectra in Fig. 5 at small spatial scales.

Wave perturbations to temperature and density. The frequency perturbations in Figs. 5–7 are caused by structure on scales smaller than the resolution of the atmospheric profiles in Fig. 4. In order to characterize this structure more completely, we retrieved additional profiles from the data at both ingress and egress. For one, we used a low-pass filter with $d = 5$ km during data analysis, yielding a profile with a vertical resolution of about 4 km. In other words, this profile was retrieved from the frequency data $f_0 + f_1'$. We derived another profile from unfiltered data (i.e., $f_0 + f_1' + f_2'$); in this case the vertical resolution was diffraction-limited to about 1 km. These two additional profiles exhibit small-scale temperature perturbations superimposed on the background structure of Fig. 4. We then computed the difference between pairs of atmospheric profiles with different vertical resolutions to isolate temperature perturbations, T', in wavelength passbands of 0–4 and 4–16 km. The results are shown in Figs. 8–11.

Our method for interpreting these data involves use of the standard, linear theory for time-harmonic atmospheric waves (see below). We therefore restricted our attention to the most prominent, quasi-sinusoidal features that appear in Figs. 6–7, which correspond to the dominant periodicities of the data (Fig. 5). Specifically, we selected for

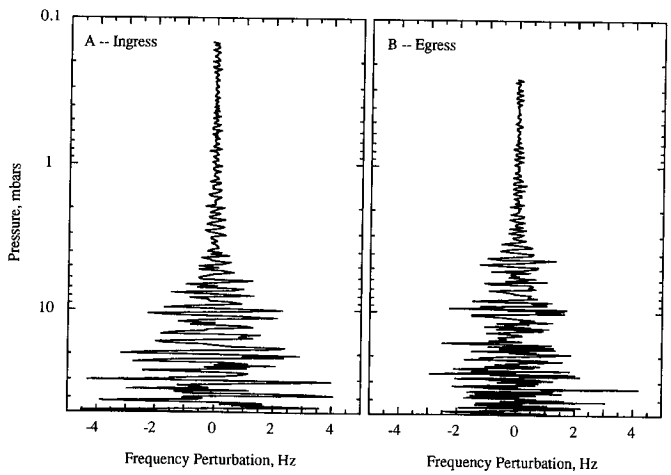

FIG. 7. Frequency perturbations, f_2', that result from atmospheric structure with vertical wavelengths smaller than 4 km. Measurements exceed the noise level at pressures greater than 2–3 mbars.

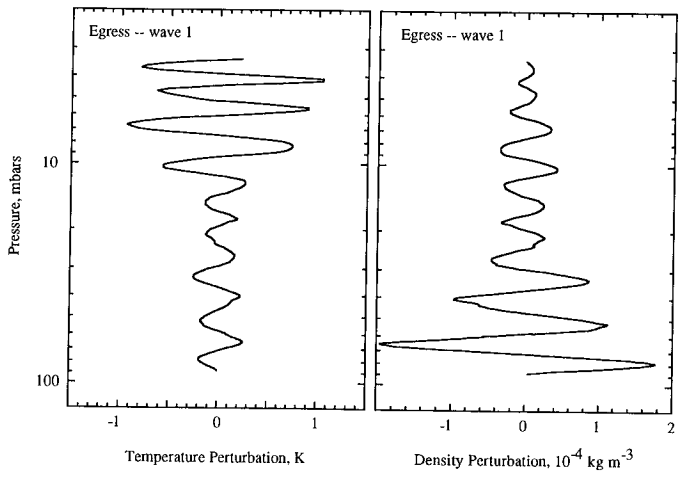

FIG. 8. Atmospheric structure on spatial scales of 4–16 km in the stratosphere at egress. There is a direct correspondence between the variations in f_1' that appear in Fig. 6b at pressures 3–90 mbars and these profiles of T' and ρ'. We will refer to this pattern of oscillations as wave 1. The pressure interval displayed here and in Figs. 9–10 corresponds to an altitude interval of about 90 km.

further analysis the oscillations in f_1' at pressures 3–90 mbars in Fig. 6b and at pressures 80–1000 mbars in Fig. 6a, as well as the oscillations in f_2' at pressures 4–40 mbars in Fig. 7a. Of necessity, we avoided the irregular or seemingly random variations in f' that are also present in Figs. 6–7, for which this simple theory seems inappropriate (e.g., the fluctuations in f_1' at pressures 2–70 mbars in Fig. 6a or in f_2' at pressures 5–50 mbars in Fig. 7b). These features might represent superpositions of waves with different vertical wavelengths, or possibly turbulent layers generated by shear instability, but in either case their interpretation is problematical and will not be considered here. Although the criteria used in selecting data for further analysis is admittedly subjective, we feel that it represents a reasonable first attempt at interpreting the principal features of the observations.

Consider first the atmospheric structure on spatial scales of 4–16 km. Figure 8 shows the perturbations T' that correspond to the sinusoidal variations in f_1' observed at pressures 3–90 mbars at egress (cf. Fig. 6b). The oscillations have an average vertical wavelength of 8 km. For comparison, the sample spacing of the measurements decreases steadily from about 800 m at 3 mbars to about 40 m at 90 mbars. The amplitude of the oscillations generally increases with height, from 0.2 K at 80 mbars to 1 K at 6 mbars. This is qualitatively consistent with the behavior expected for a freely propagating atmospheric wave. We note once again the sensitivity of the measurements: a wave with an amplitude of only 0.2 K can produce an easily detectable perturbation to received signal frequency.

Figure 8 also shows the vertical profile of density perturbations, ρ'. This is the more fundamental measurement in a radio occultation experiment since $\rho \propto \mu - 1$ (for a homogeneous mixture of H_2 and He) while T is obtained through vertical integration of ρ [cf. Eq. (10) of Fjeldbo and Eshleman 1968]. However, atmospheric waves are usually characterized in terms of temperature rather than density perturbations. In addition, the relationship between T' and ρ' is straightforward for the method of data analysis used here:

$$T' \approx -T_0 \frac{\rho'}{\rho_0}. \tag{4}$$

Here, ρ_0 and T_0 refer to the background structure of the atmosphere (Fig. 4), and we have assumed that $T'/T_0 \ll 1$, which is easily satisfied. For these reasons, profiles of ρ' are not shown in subsequent figures.

Figure 9 shows the perturbations T' observed in the troposphere at ingress over the same range of spatial scales. The observations extend to a pressure near 1000

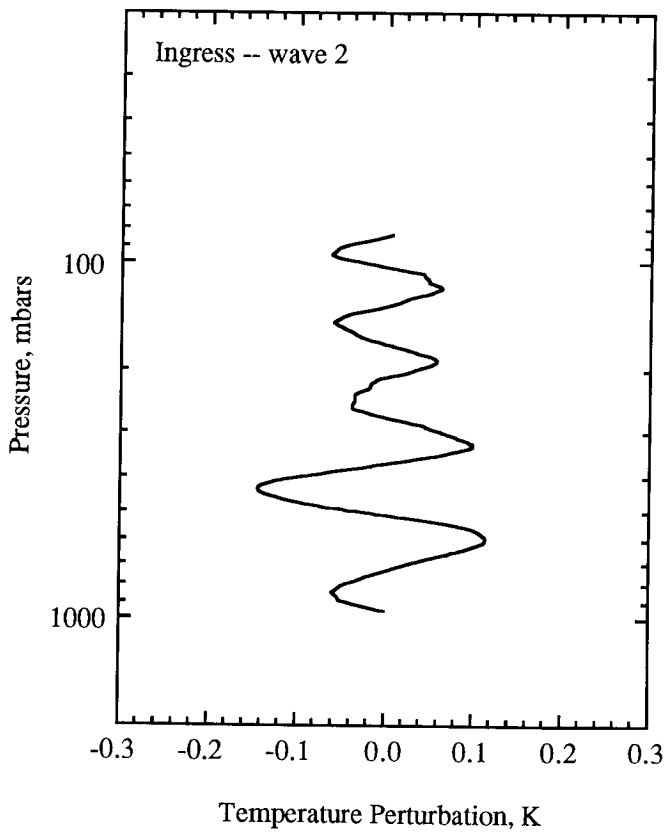

FIG. 9. Atmospheric structure on spatial scales of 4–16 km in the troposphere at ingress (wave 2), corresponding to the variations in f_1' that appear in Fig. 6a at pressures 80–1000 mbars. This profile of T' was obtained from frequency measurements with a sampling rate of 6.10 Hz.

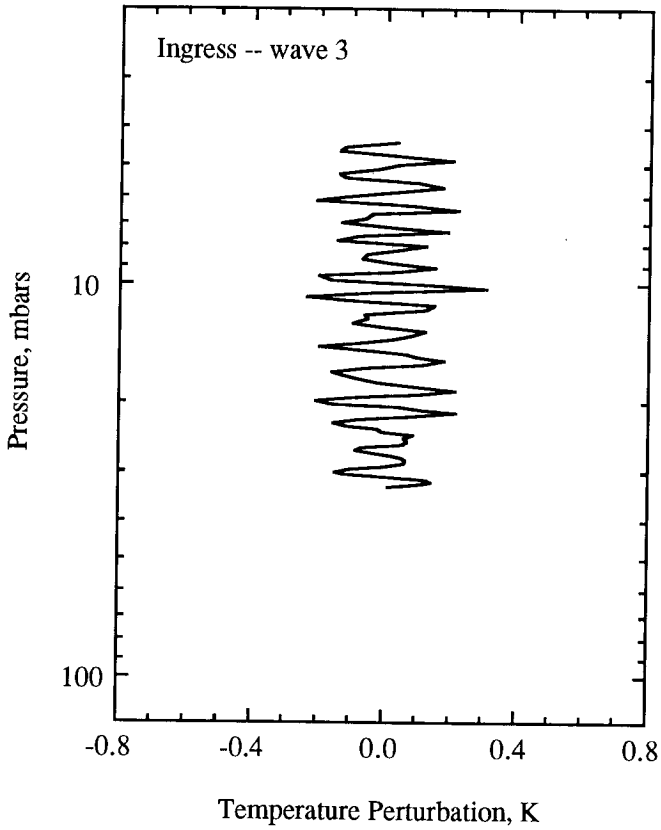

FIG. 10. Atmospheric structure on spatial scales smaller than 4 km in the stratosphere at ingress (wave 3), corresponding to the variations in f_2' that appear in Fig. 7a.

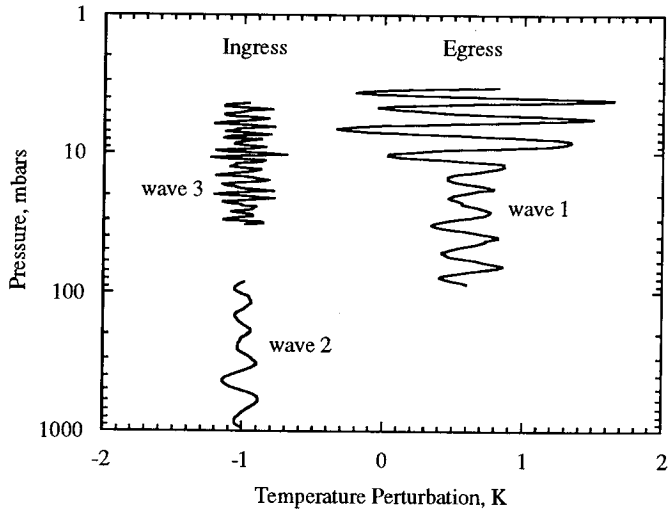

FIG. 11. Temperature perturbations from Figs. 8–10 superimposed on the same axes. Arbitrary temperature offsets have been introduced to avoid overlap.

mbars, within about 15 km of the CH_4 condensation level (Lindal 1992). The corresponding variations in f_1' were noted previously in Fig. 6a. These oscillations in temperature have an average vertical wavelength of 9 km. The sample spacing of the measurements decreases from about 200 m at 80 mbars to about 90 m at 900 mbars.

Figure 10 shows analogous results at ingress for atmospheric structure on spatial scales smaller than 4 km. The oscillations in T' have an average vertical wavelength of 3 km, corresponding to the highest spectral peak in Fig. 5a and the prominent oscillations in f_2' in Fig. 7a. The amplitude in temperature is about 0.2 K throughout this pressure interval. The sample spacing of the measurements decreases from about 700 m at 4 mbars to about 300 m at 30 mbars.

In summary, Fig. 11 shows the temperature perturbations from Figs. 8–10 superimposed on the same axes. Table III lists basic characteristics of the three putative waves.

Constraints on horizontal structure. In deriving the results shown in Figs. 5–11, we assumed that any wave-induced horizontal variations in atmospheric structure had a negligible effect on the measurements. We now assess the impact of this assumption on the reliability of these results and, at the same time, derive a constraint on the horizontal structure of the waves.

We will consider the effect on radio occultation measurements of a generic atmospheric wave whose structure in local, Cartesian coordinates is given by

$$\rho'(x, y, z, t) = Ae^{-z/2H} \exp[i(kx + ly + mz - \omega t)]. \quad (5)$$

Here, A is a constant, ω is the wave frequency, and the wave vector $\mathbf{k}$ has components k, l, and m in the zonal,

TABLE III
Measured Wave Properties

Parameter	Wave 1	Wave 2	Wave 3
Location:			
Latitude	45°S	61°N	61°N
Longitude	130°E	221°E	223°E
Pressure[a] (mbars)	3–90	80–1000	4–40
Average vertical wavelength[a] ($2\pi/m$) (km)	8	9	3
Amplitude in temperature[a] (K)	0.2–1	~0.1	~0.2
Figure showing vertical structure	8	9	10
Aspect ratio, $m/k_\parallel$	>17	>20	>17

[a] Estimate based on neglect of horizontal structure of wave.

meridional, and vertical directions, respectively. This expression can be generalized to spherical coordinates by setting

$$x \rightarrow r_0 \cos\phi\,(\Lambda - \Lambda_0)$$
$$y \rightarrow r_0(\phi - \phi_0) \qquad (6)$$
$$z \rightarrow r - r_0.$$

Here, r is radius, Λ is east longitude, and ϕ is planetographic latitude; r_0, Λ_0, and ϕ_0 are reference values. At an arbitrary location, the generalized wave vector $\mathbf{k}$ has local horizontal and vertical components $\mathbf{k}_h \equiv (k, l, 0)$ and $\mathbf{k}_v \equiv (0, 0, m)$, respectively.

We can relate the spatial structure of the wave to the experiment geometry by defining a unit vector $\mathbf{s}$ that is tangent to the ray path at the proximate point. The angle between $\mathbf{s}$ and the local zonal (eastward) direction on Neptune was 53° at ingress and 32° at egress. In the discussion that follows, we refer to the components of $\mathbf{k}_h$ that are parallel and perpendicular to $\mathbf{s}$ as $k_\parallel$ and $k_\perp$, respectively.

In the limit where $\mathbf{k}_h \rightarrow 0$, ρ' is independent of Λ and ϕ. Reliable measurements of the vertical wavelength ($2\pi/m$) and the vertically varying wave amplitude ($Ae^{-z/2H}$) can then be retrieved through use of the Abel transform, which is based on the assumption of local spherical symmetry. This situation is depicted in Fig. 12a. However, when $\mathbf{k}_h \neq 0$, this assumption is no longer valid and two types of errors can appear in results derived with the Abel transform.

The first type of error is attributable to $k_\parallel$ and affects estimates of wave amplitude and location. When $k_\parallel \neq 0$, the radio signals propagating from spacecraft to Earth encounter sinusoidal variations in wave structure *beyond what would be expected for a spherically symmetrical atmosphere,* as shown in Fig. 12b. There is nearly complete cancellation between the perturbations caused by successive wave crests and troughs in some regions, but strong coupling between the wave and the radio signal can still occur at preferred locations. Model calculations, described below, show that the Abel transform can accurately recover the spatial pattern of density perturbations, ρ', for both cases illustrated in Fig. 12. However, when $k_\parallel \neq 0$, as in Fig. 12b, the Abel transform attributes the signal perturbations to structure like that shown in Fig. 12a, yielding a profile of ρ' that is shifted lower in altitude relative to its true location. This in turn causes incorrect values for ρ_0 and T_0 to be used in evaluating the right-hand side of Eq. (4), leading to errors in the estimate of T'. The error caused by ρ_0 will generally dominate because of the exponential variation of ρ_0 with height. As the profile of ρ' can be shifted only downward, the value of ρ_0 used in Eq. (4) will always be too large. By neglecting to account for this effect, the Abel transform will underestimate T' unless $k_\parallel$ is sufficiently small. The results in Figs. 8–11 and Table III therefore represent lower bounds on T'.

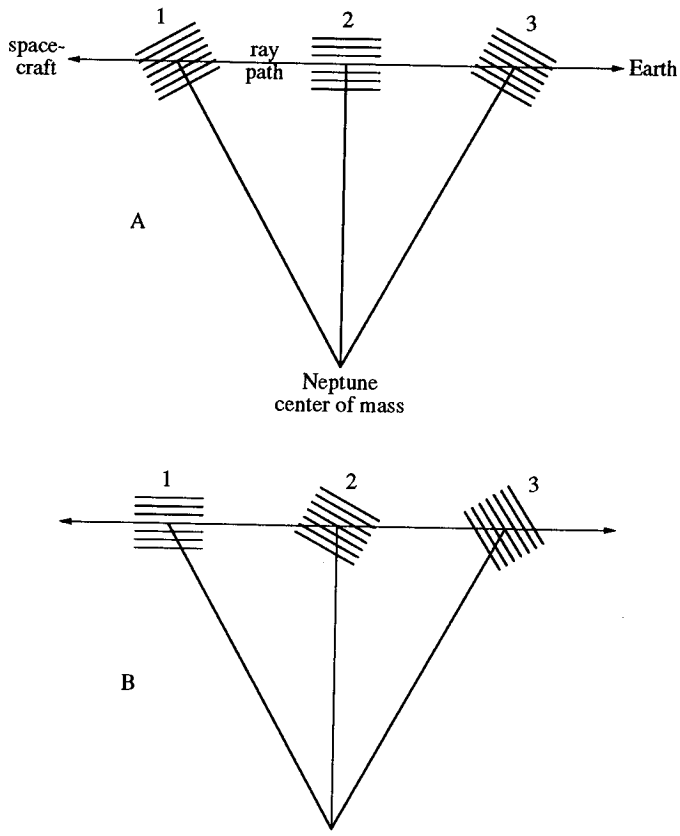

FIG. 12. Schematic showing orientation of ray path relative to striations of atmospheric density. For simplicity, the ray path is depicted as a straight line. In (A), the density striations are aligned with the local horizon. The net effect on the radio signal from regions 1 and 3 is negligible, since there is nearly complete cancellation between perturbations caused by successive crests and troughs of the density variations. In contrast, the striations in region 2 produce a strong cumulative effect on the radio signal. Vertical motion of the ray path through this type of "onion-layer" atmospheric structure produces oscillations in signal frequency that can be interpreted correctly with the Abel transform. In (B), each "packet" of striations has been rotated clockwise by about 30° relative to (A). Viewed locally, the striations have a horizontal-to-vertical aspect ratio of $\sqrt{3}$. Cancellation now occurs in regions 2 and 3, but the net effect of the striations on the radio signal can still be appreciable because of the interaction in region 1. However, attempts to interpret the signal perturbations with the Abel transform will produce errors (see text).

We characterized the behavior of this error source through use of numerical simulations. We began by constructing a model atmosphere consisting of isothermal background structure modulated by an atmospheric wave of the form given by Eqs. (5) and (6). We then calculated the effect of the wave on radio occultation measurements by applying standard formulas of geometrical optics (Born and Wolf 1975). We repeated these steps using a range

of values for wave parameters. We found that the errors are relatively small when $2\pi/k_{\|}$ exceeds $2\pi/m$ by a factor of 50. In that case, the spatial pattern of density perturbations obtained with the Abel transform is shifted downward by about 5 km and the estimate for T' is about 20% less than its true value. However, when the aspect ratio $m/k_{\|}$ is reduced to 20, the vertical shift increases to about 30 km and the estimate for T' is too small by a factor of about 3. Both the shift in altitude and the error in T' increase rapidly with further decreases in $m/k_{\|}$. These results are nearly independent of the value of $2\pi/m$, at least over the range of values considered here.

We are now in a position to obtain a constraint on $k_{\|}$ by deriving an upper bound on the wave amplitude. To avoid a convective instability,

$$\left|\frac{dT'}{dz}\right| < \frac{N^2 H}{R}. \tag{7}$$

When $m \gg 1/2H$, which applies here, this condition becomes

$$|T'| < \frac{N^2 H}{mR}. \tag{8}$$

This upper bound on $|T'|$ allows us to place an upper limit on the amount by which the true wave amplitude can exceed the estimate obtained from the Abel transform. We applied Eq. (8) to the waves shown in Figs. 8–10 using measured values for N, H, and m. For example, the true amplitude of wave 3 (Fig. 10) cannot exceed 0.9 K at the 10-mbar pressure level; this upper bound exceeds the nominal measured value by a factor of about 4. When combined with the results from the numerical simulations described above, this condition leads to the conclusion that $m/k_{\|} > 17$ for this wave. Table III gives the constraint on $m/k_{\|}$ obtained in this manner for each wave.

The Abel transform is susceptible to a second type of error, which arises from $k_{\perp}$ and affects measurements of the vertical wavelength ($2\pi/m$). It can occur when the experiment geometry involves horizontal motion of the ray path (i.e., when the latitude and/or longitude of the proximate point varies with pressure). This was the case in the occultation of Voyager 2 by Neptune, as shown in Fig. 13. The ray path sliced obliquely through the atmosphere, sampling both vertical and horizontal variations in wave structure. The angular frequency of the resulting oscillations in f' is given by

$$\kappa = v_v m + v_h k_{\perp}. \tag{9}$$

Here, v_v and v_h are the vertical and horizontal components, respectively, of ray path velocity relative to the atmosphere. (The steps of data analysis that led to Fig. 13 also yielded estimates for v_v and v_h.) Obviously, measurements of κ are not sufficient to yield unique solutions for both m and $k_{\perp}$. Our estimates for $2\pi/m$ in Table III, which are based on the assumption that $k_{\perp} = 0$, are therefore subject to a possible bias.

The size of the error from this source is determined by the experiment geometry (Fig. 13) and the spatial structure of the wave. Consider first the measurements at ingress. At pressures less than 30 mbars in the stratosphere, the ray path moved at nearly the same rate in the horizontal and vertical directions. From Eq. (9), the fractional error in $2\pi/m$ will therefore have a magnitude of about $k_{\perp}/m$. At pressures exceeding 300 mbars in the troposphere, the proximate point moved about 20 times more rapidly in the horizontal direction than the vertical direction, leading to a fractional error in $2\pi/m$ of about $20 \times k_{\perp}/m$. The corresponding fractional errors for measurements at egress are about $k_{\perp}/m$ and $50 \times k_{\perp}/m$. These simple geometrical considerations lead to the following conclusions. For the waves in the stratosphere (Figs. 8 and 10), this error source will have a relatively small impact on the estimates of $2\pi/m$ provided that $k_{\perp} \ll m$. For example, if $k_{\perp} \approx k_{\|}$, which seems plausible, the error in $2\pi/m$ would be less than 6% (cf. Table III). In contrast, the estimate of $2\pi/m$ for the wave in the troposphere (Fig. 9) is subject to much greater uncertainty. For this reason, we will restrict subsequent discussion to the waves observed in the stratosphere.

DISCUSSION

In this section we consider the question of wave identity and derive constraints on wave frequency and horizontal phase speed. We infer other general properties of the waves by modeling their measured vertical structure. We then discuss the possible impact of the waves on the eddy mixing, circulation, and thermal structure of the middle atmosphere.

We focus our attention on waves 1 and 3, whose vertical wavelengths can be estimated reliably. To simplify the interpretation, we will assume that: (1) each feature can be modeled accurately as a single, time-harmonic wave mode; (2) the wave source is in the convective lower troposphere, so that the vertical component of the group velocity is upward throughout the pressure range of the measurements; and (3) the wave motion is hydrostatic (i.e., $m \gg k, l$; Gill 1982), as implied by the constraints on $m/k_{\|}$ in Table III. The first assumption is the most questionable of the three. Recall that the profiles of T' in Figs. 8 and 10 represent measurements within wavelength passbands of about 4–16 and 0–4 km, respectively. Each measured profile could therefore contain a superposition of waves with different amplitudes and vertical wave-

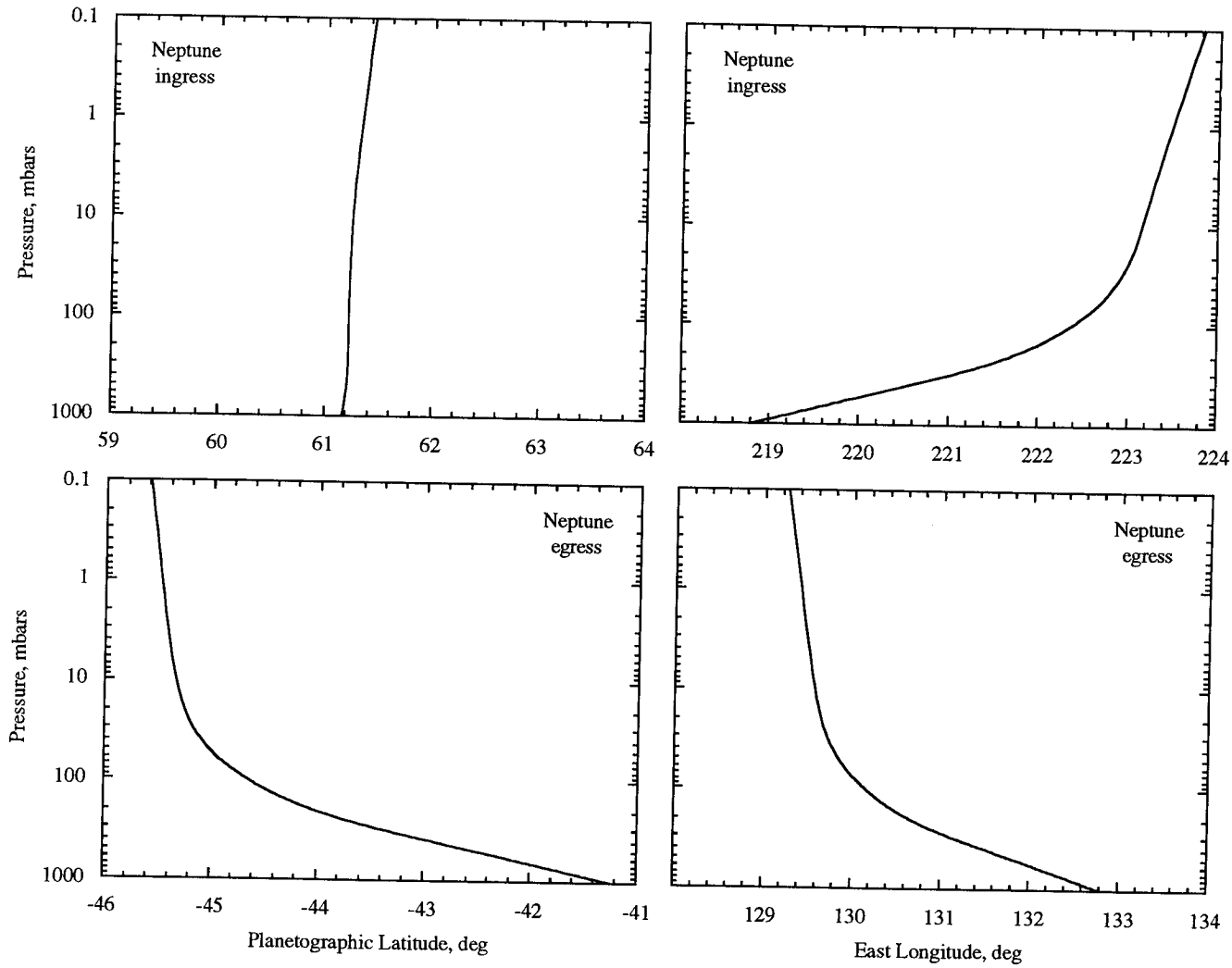

FIG. 13. Latitude and longitude vs pressure for the proximate point on the ray path. This characterization of the experiment geometry was obtained as a natural byproduct of the analysis that led to the results in Fig. 4. The bend that appears near the 100-mbar pressure level in three of the curves is a consequence of the spacecraft trajectory and the exponential increase in α with decreasing a. See Connerney *et al.* (1991) for a definition of the longitude system.

lengths. Judging by the appearance of the spectrum in Fig. 5a, this is a serious possibility for wave 3. However, the situation is ambiguous for wave 1, where the spectral broadening of the main peak in Fig. 5b could be due either to a superposition of modes with nearly the same vertical wavelength, or to the variation of m with height that is expected for a single, monochromatic wave (see below). We adopted assumption 1, above, in the interest of finding the simplest possible interpretation for the data. This comes at the expense of introducing some uncertainty into our results and conclusions.

Wave identity, frequency, and horizontal phase speed. Among the classes of waves that could be present at mid-latitudes on Neptune, Rossby waves and inertio-gravity waves are the best candidates for explaining the observations.[4] Our first challenge is to resolve this uncertainty in the wave identity.

To model the behavior of Rossby waves, we used quasi-geostrophic theory (which excludes inertio-gravity waves), a beta-plane geometry, and a coordinate system rotating at angular rate $\Omega = 1.083 \times 10^{-4}$ sec^{-1}, the rotation rate of Neptune's internal magnetic field (Warwick *et al.* 1989). We considered only the case where $m \gg 1/2H$, which is appropriate here. We also linearized the basic fluid equations; the validity of this approxima-

[4] In principle, acoustic waves are another possibility, but their periods are shorter than those of inertio-gravity and Rossby waves, and little natural excitation is expected at these frequencies. See French and Gierasch (1974) for additional arguments opposing an acoustic-wave interpretation.

tion is considered below. Within this theoretical framework, Rossby waves propagating on a basic zonal flow obey the following dispersion relation (Andrews *et al.* 1987):

$$\sigma_i \equiv \omega - k\bar{u} = \frac{-\beta k}{k^2 + l^2 + m^2 f^2/N^2}. \tag{10}$$

Here, σ_i is the intrinsic frequency, $\bar{u}$ is the mean zonal wind speed, the Coriolis parameter $f \equiv 2\Omega \sin \phi$, and $\beta \equiv df/dy$. Table II gives values for f and β at the latitudes of interest. Although Eq. (10) is strictly valid only when $\bar{u}$ and N are constants, it remains accurate when these two parameters vary slowly with position.

In the present application, the only unknowns in this expression for σ_i are k and l, the horizontal components of the wave vector. Hence, two conditions must be satisfied if the observed waves are Rossby waves[5]:

$$|\sigma_i| \leq \frac{N\beta}{2|mf|} \tag{11}$$

$$|c| \leq \frac{N^2\beta}{m^2 f^2}. \tag{12}$$

Here, $c \equiv \sigma_i/k$, the zonal phase speed measured relative to $\bar{u}$ (with eastward positive). Substituting measured values for N, f, β, and m appropriate to wave 1:

$$|\sigma_i| \leq 5 \times 10^{-7}\ \text{sec}^{-1} < \Omega/200 \tag{13}$$

$$|c| \leq 0.15\ \text{m sec}^{-1}. \tag{14}$$

Tighter constraints apply for wave 3. Hence, Rossby waves with the vertical structure shown in Figs. 8 and 10 would have small zonal phase speeds (relative to $\bar{u}$) and long periods.

Consider the behavior of Rossby waves when $\bar{u}$ varies with height but not latitude. By Eq. (10), a Rossby wave propagating through vertical wind shear experiences a Doppler shift in its intrinsic frequency, which produces commensurate changes in the vertical wavenumber m. (Note that ω, k, and l are independent of height in this simple case.) When the vertically integrated wind shear is comparable to or greater than $|c|$, the wave would be expected to exhibit substantial vertical variations in m. However, effects of this type are not apparent in the data, even though the vertical wind shear on Neptune inferred from Voyager 2 IRIS observations is typically of order 10 m sec^{-1} per scale height near the tropopause (Conrath *et al.* 1991a). Specifically, the value of m for waves 1 and 3 varies by less than 50% over a height interval where the vertically integrated wind shear exceeds the upper bound on $|c|$ by a factor of 50 or more. For this reason, it is difficult to reconcile the observations with a Rossby-wave interpretation.

[5] These conditions follow from the functional dependence of σ_i on k and l. for example, $|\sigma_i|$ achieves its largest value, given in Eq. (11), when $l \to 0$ and $k^2 = (mf/N)^2$ (cf. Fig. 2 of French and Gierasch 1974).

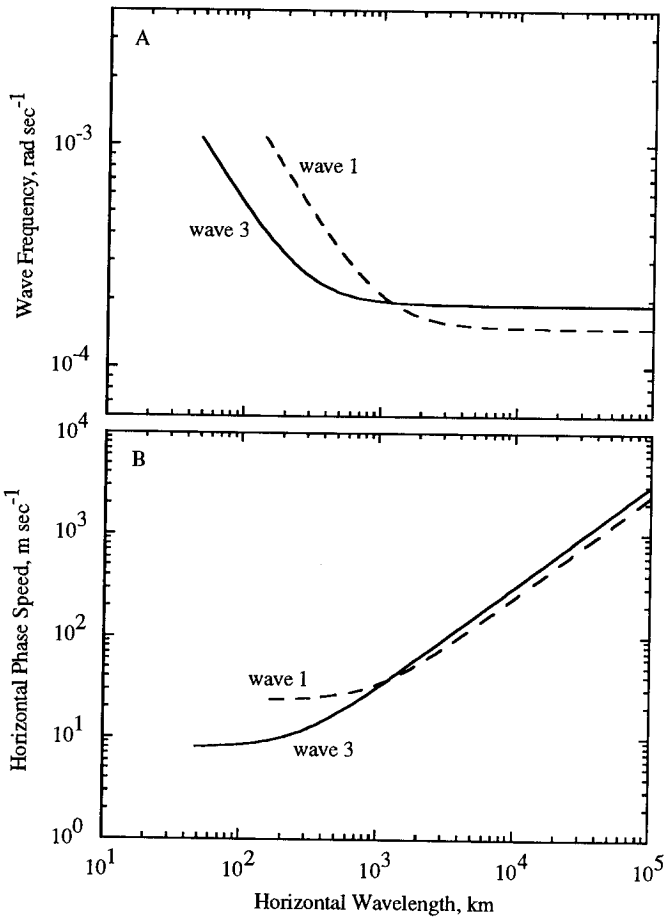

FIG. 14. Predictions of theory for inertio-gravity waves applied to the observations. We used measured values for N, f, and m in Eq. (15) to compute the intrinsic frequency, σ_i, and the horizontal phase speed, σ_i/k_h, as functions of the horizontal wavelength, $2\pi/k_h$. Results are shown for waves 1 (dashed line) and 3 (solid line) of Table III.

We modeled the behavior of inertio-gravity waves using linear equations of motion and an f-plane geometry (which excludes Rossby waves). These assumptions lead to the following dispersion equation (Andrews *et al.* 1987):

$$\sigma_i \equiv \omega - k\bar{u} = \left(f^2 + \frac{N^2(k^2 + l^2)}{m^2}\right)^{1/2}. \tag{15}$$

We used this expression along with measured values for N, f, and m to compute σ_i and the *horizontal* phase speed, σ_i/k_h, as functions of the horizontal wavelength, $2\pi/k_h$, where $k_h \equiv (k^2 + l^2)^{1/2}$. Figure 14 shows the results. We

TABLE IV
Inferred Wave Properties

Parameter	Wave 1	Wave 3	Units
Wave identity	Inertio-gravity	Inertio-gravity	
Intrinsic frequency, $\lvert\sigma_i\rvert$	1.5–11	1.9–11	10^{-4} sec^{-1}
Zonal phase speed, $\lvert c\rvert$	>23	>8	m sec^{-1}
Breaking level, p_b	0.5	3	mbars
Strong attenuation level, p_a	1	15	μbars
Eddy diffusivity, K_e ($p_a < p < p_b$)	<50	<2	m^2 sec^{-1}
Wave forcing of the mean flow, $\lvert\partial\bar{u}/\partial t\rvert$ ($p_a < p < p_b$)	<9	<3	m sec^{-1} per planet rotation

considered values for $2\pi/k_h$ ranging from 17 times the observed vertical wavelength (cf. Table III) to 10^5 km, roughly the circumference of a latitude circle at mid-latitudes.

By Eq. (15), $|\sigma_i| > |f|$ for inertio-gravity waves. In addition, Fig. 14b shows that $|\sigma_i/k_h|$ exceeds 23 and 8 m sec^{-1} for waves 1 and 3, respectively. The same conditions apply to the *zonal* phase speed, since $|c| \geq |\sigma_i/k_h|$. These constraints on σ_i and c contrast with the corresponding results for Rossby waves. With their much larger zonal phase speeds, inertio-gravity waves are far less susceptible than Rossby waves to the effects of wind shear. In this regard, the behavior of inertio-gravity waves is compatible with the observations.

We conclude that the waves in Figs. 8 and 10 are most likely inertio-gravity waves. In summary, Fig. 14 gives the plausible range of values for the wave frequency and horizontal phase speed. The constraints on σ_i and c are listed in Table IV.

Wave vertical structure. Within the theoretical framework described above, and in the absence of dissipation, the vertical structure of a linear, inertio-gravity wave is given approximately by

$$T' \propto T_0 \left(\frac{N^3}{\rho_0}\right)^{1/2} \exp\left[i \int^z m\, dz'\right]. \qquad (16)$$

Here, N, T_0, and ρ_0 refer to the background structure, and the effect of wind shear has been ignored. This expression corresponds to a WKB solution to the vertical structure equation. [See Lindzen (1981) or Hinson and Magalhães (1991) for analogous results that apply to pure internal gravity waves and equatorial waves, respectively.] From Eq. (16), the amplitude of the temperature oscillations is expected to increase with height basically as $\rho_0^{-1/2}$, but with additional modulation resulting from the vertical variations in N and T_0. The theory also predicts that m varies with height in such a way that

$$N/m = \text{constant}. \qquad (17)$$

The value of the constant corresponds to the horizontal phase speed of an equivalent pure internal gravity wave [cf. Eq. (15) in the limit $f \rightarrow 0$].

This theoretical expression for T' has three free parameters: the ratio N/m, and the amplitude and phase of the temperature oscillations at a reference pressure level. Figure 15 shows our attempt to match the theory to the observed vertical structure of waves 1 and 3. Both the phase and amplitude of the temperature oscillations in Fig. 15a show good qualitative agreement with the observations in Fig. 8. Thus, wave 1 can be interpreted plausibly as a linear, time-harmonic wave mode. In contrast, the theoretical profile in Fig. 15b differs markedly from the observations in Fig. 10. Wave 3 appears to be saturated (i.e., the amplitude of the observed temperature oscillations does not increase appreciably with height), possibly due to the onset of dissipation (see below).

A closer comparison of the profiles in Figs. 8 and 15a reveals subtle differences in the predicted and observed variations of m with height. There are several possible

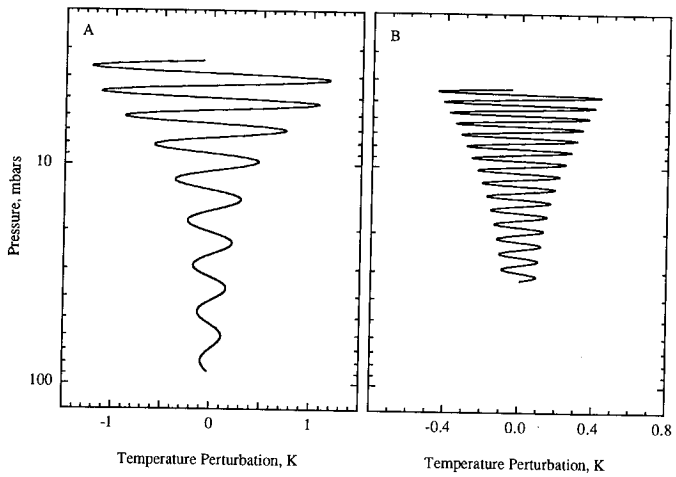

FIG. 15. Theoretical profiles of wave-induced temperature perturbations computed from Eqs. (16)–(17). The two profiles represent an attempt to match predictions of theory to the observed vertical structure of waves 1 and 3 (cf. Figs. 8 and 10). The ratio N/m was assigned values of 23 and 8 m sec^{-1} for (A) and (B), respectively. In each case, this choice of N/m yields the same number of temperature oscillations as was observed in the pressure range of interest. In all calculations we used measured profiles of N, T_0, and ρ_0 that were derived from the radio occultation data.

explanations for this discrepancy. For example, it could reflect the influence of vertical wind shear, as described earlier in the discussion of wave identity, which was ignored in Eq. (16). In principle, estimates for the wind shear could be obtained by fitting more sophisticated models for the vertical structure to the data. Alternatively, the discrepancy could result from the altitude bias in the measured wave profile that occurs when the wave horizontal-to-vertical aspect ratio is relatively small. In this case, the ambient values for N, T_0, and ρ_0 used in the model calculations would be inappropriate to the observations. Finally, the differences between the measured and predicted variations in m could be due to modulation caused by the presence of several wave modes with different amplitudes and vertical wavelengths. However, a more detailed analysis of the observed vertical structure is beyond the scope of this paper.

Wave dissipation. The exponential growth of wave amplitude with height predicted by Eq. (16) cannot persist above the so-called breaking level, where the combination of wave and mean temperature fields yields an adiabatic lapse rate [cf. Eq. (8)]. At altitudes above this level, the wave triggers overturning, convection, and small-scale turbulence which prevent further growth in wave amplitude. In this way, atmospheric waves can produce mechanical mixing in otherwise stably stratified regions of the atmosphere, with important implications for the transport of minor constituents.

For wave 1, the measured temperature lapse rate appears to be subadiabatic, despite the wave perturbations, throughout the pressure range of the observations. Estimates of the pressure at the breaking level, p_b, therefore require extrapolation. Toward this end, we used Eq. (16) with constraints from the measurements to model the vertical structure of the wave (cf. Fig. 15a). This model combined with Eq. (8) predicts that $p_b \approx 0.5$ mbars for wave 1.

The behavior of wave 3 is basically different and possibly more revealing. The absence of the expected increase in wave amplitude with height suggests that dissipation is already occurring within the interval of direct observations. This interpretation implies that the horizontal-to-vertical aspect ratio for wave 3 must have a value of roughly 17, the lower bound given in Table III, so that the inferred amplitude of the wave would be sufficient to produce a convective instability. Taking into account the bias in height (~40 km) that would occur for this value of the aspect ratio, we estimate that $p_b \approx 3$ mbars for wave 3.

Our next task is to model the process of dissipation, which occurs at pressures less than p_b. In a widely used approach to this problem, wave breaking is assumed to generate spatially uniform, *small-scale* eddy mixing that acts to attenuate the wave in a manner akin to molecular

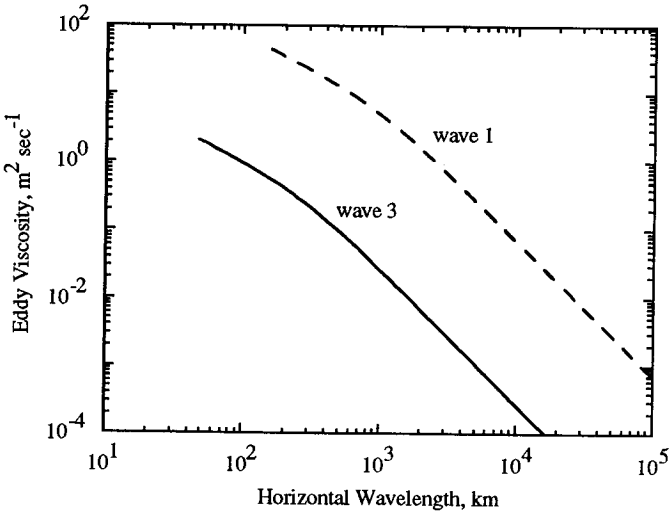

FIG. 16. Predictions of linear theory for inertio-gravity waves applied to the observations. We used measured values for N, H, f, and m in Eqs. (18) and (15) to compute the eddy diffusion coefficient, K_e, as a function of the horizontal wavelength, $2\pi/k_h$. These results correspond to the so-called Lindzen parameterization.

viscosity. To avoid superadiabatic lapse rates, dissipation presumably drives the eddy diffusion coefficient, K_e, to a value sufficient to offset the tendency for exponential growth of wave amplitude with height (cf. Hodges 1969, Hines 1970). The eddy diffusivity produced in this way by a linear inertio-gravity wave is given by (cf. French and Gierasch 1974, Lindzen 1981):

$$K_e = -\frac{\sigma_i^2 - f^2}{2H\sigma_i m^3}. \tag{18}$$

This approach to estimating K_e, sometimes called the Lindzen parameterization, has gained wide acceptance because of its simplicity (e.g., Fritts 1984). We used Eqs. (18) and (15) with measured values for N, H, f, and m to compute K_e as a function of $2\pi/k_h$ for waves 1 and 3. The results appear in Fig. 16. Within the constraints on m/k_h in Table III, K_e could be as large as 50 and 2 m^2 sec^{-1} for waves 1 and 3, respectively.

Near the breaking level, the molecular viscosity of the H_2–He mixture, K_m, is relatively small compared to the computed values for K_e, and its effect on the wave can be ignored. However, this is not the case at lower pressures since K_m increases exponentially with height, reaching a value of about 3 m^2 sec^{-1} at a pressure of 10 μbars. A wave propagating upward will experience exponentially increasing attenuation due to molecular viscosity. At the level where $K_m \approx K_e$, which we denote by its pressure p_a, this damping is sufficient to suppress wave breaking. For example, if $m/k_h = 20$, p_a is about 1 and 15 μbars

for waves 1 and 3, respectively. Hence, within this simple theoretical framework, K_e is expected to be roughly constant at pressures between p_b and p_a but negligible outside this region.

Despite its widespread use, the Lindzen parameterization has serious flaws. For example, linearized equations are being used to model a process that is inherently nonlinear (Andrews *et al.* 1987, pp. 193–194). In addition, the exponential growth of wave amplitude results in unstable stratification only within localized regions, so that use of a spatially uniform eddy diffusion coefficient is inappropriate (Coy and Fritts 1988). These and other problems have been discussed by Walterscheid and Schubert (1990), who used numerical simulations to study the nonlinear evolution of an upward propagating internal gravity wave. They identified the mechanism responsible for limiting the growth of the wave as the overturning of surfaces of constant potential temperature. Breakdown occurs in the form of cellular convection driven by the resulting unstable potential temperature gradients. As this process cannot be modeled adequately through use of an eddy diffusion formalism (Fritts and Dunkerton 1985, Coy and Fritts 1988), Walterscheid and Schubert concluded that the Lindzen parameterization has no rigorous justification. For these reasons, our estimates of K_e are rough approximations at best. We decided to apply Eq. (18) despite its limitations because of the importance of this parameter in photochemical models.

Finally, it is instructive to compare our results with two independent estimates for K_e. First, Bézard *et al.* (1991) studied Voyager 2 observations of infrared emission from Neptune in the acetylene and ethane bands; these measurements pertain to pressures between about 0.03 and 3 mbars. Their photochemical models show best agreement with the disk-averaged data when $K_e \approx 10$ m^2 sec^{-1} at the 1-mbar pressure level. Second, Bishop *et al.* (1992) analyzed solar occultation data at wavelengths of 125–138 nm obtained with the Voyager 2 UVS instrument. In the occultation geometry, absorption by methane attenuates solar radiation at these wavelengths to 50% of its free-space intensity at a pressure near 0.2 μbars. Predictions from photochemical models show best agreement with the UVS "lightcurves" when $K_e \approx 10^3$ m^2 sec^{-1} at this pressure level. These results are close enough to values given here to suggest that wave breaking is a significant source of eddy mixing in the middle atmosphere of Neptune. Hinson and Magalhães (1991) reached the same conclusion in a previous study of atmospheric waves on Uranus.

Effect of the waves on the background circulation and thermal structure. The effect of an atmospheric wave on the mean zonal circulation can be expressed as [cf. Eqs. (3.5.1)–(3.5.3) of Andrews *et al.* 1987]

$$\frac{\partial \bar{u}}{\partial t} \approx e^{\hat{z}} \frac{\partial F^{(\hat{z})}}{\partial \hat{z}}, \tag{19}$$

where

$$F^{(\hat{z})} \equiv e^{-\hat{z}} \left(f \frac{\overline{v'\theta'}}{\partial \bar{\theta}/\partial \hat{z}} - \overline{\hat{w}'u'} \right). \tag{20}$$

Here, $\hat{z}$ is a log-pressure vertical coordinate (dimensionless); $F^{(\hat{z})}$ is the vertical component of the Eliassen–Palm flux (EP flux); u, v, and $\hat{w} \equiv d\hat{z}/dt$ are the eastward, northward, and upward components, respectively, of fluid motion; and θ is potential temperature. An overbar denotes a zonal average, while primed quantities represent wave perturbations. The first term in the expression for $F^{(\hat{z})}$ represents the effect of the Eulerian-mean circulation induced by the wave, while the second corresponds to eddy forcing. We have simplified Eqs. (19)–(20) by neglecting wind shear, mechanical dissipation (e.g., due to eddy viscosity), advection, and the y-component of the EP flux. The available data are not sufficient for evaluation of such effects. Nevertheless, Eqs. (19)–(20) should be sufficient for obtaining a simple first approximation to $\partial \bar{u}/\partial t$ [cf. Eq. (8.3.3) of Andrews *et al.* 1987].

We now apply these results within the framework of the linear theory for inertio-gravity waves. Equations (19)–(20) show that the mean zonal wind is unaffected by a steady, conservative wave (Andrews *et al.* 1987), so that $\partial \bar{u}/\partial t = 0$ for $p > p_b$. However, in the presence of dissipation, Eq. (19) becomes [cf. Eq. (24) of Lindzen 1981]:

$$\frac{\partial \bar{u}}{\partial t} \approx -\frac{N^2 k}{2Hm^3} = -\frac{N^2}{2Hm^2} \frac{k}{\sigma_i} \frac{\sigma_i}{m}. \tag{21}$$

The right-hand side is to be evaluated at the breaking level. In deriving Eq. (21), we assumed that the wave amplitude remains constant above the breaking level. As $\sigma_i/m < 0$ for a wave whose group velocity is upward, $\partial \bar{u}/\partial t$ has the same sign as σ_i/k, the zonal phase speed measured relative to $\bar{u}$. Moreover, the only unknown in this expression for $\partial \bar{u}/\partial t$ is k, the zonal wavenumber, which illustrates the importance of obtaining some measure of or constraint on the horizontal wave structure. At greater altitudes ($p < p_a$), the wave is heavily attenuated by molecular viscosity, wave amplitude decreases rapidly with height, and wave forcing of the mean flow again becomes negligible. In summary, we expect $\partial \bar{u}/\partial t$ to be roughly constant, with the value given by Eq. (21), at pressures between p_b and p_a.

Using parameter values appropriate to waves 1 and 3, Eq. (21) yields

$$\left|\frac{\partial \bar{u}}{\partial t}\right| \approx \begin{cases} 150(k/m)\ \text{m sec}^{-1}\ \text{ppr} & \text{(wave 1)} \\ 50(k/m)\ \text{m sec}^{-1}\ \text{ppr} & \text{(wave 3),} \end{cases} \quad (22)$$

where ppr means per planet rotation. Table IV lists the corresponding upper bounds on $|\partial\bar{u}/\partial t|$ based on our earlier inferrence that $m/k > 17$. Although the sign of the acceleration is unknown, its magnitude could easily be sufficient to have a significant effect on Neptune's atmospheric circulation.

As with the zonal circulation, the background thermal structure is unaffected by a steady, linear, conservative wave (i.e., $\partial\bar{T}/\partial t = 0$). However, the divergence of the EP flux that accompanies dissipation drives a "residual mean meridional circulation" whose vertical component leads directly to adiabatic heating or cooling [cf. Eqs. (3.5.1)–(3.5.2) or (7.2.1) of Andrews *et al.* 1987, Leovy *et al.* 1991]. The effect on the thermal structure can be substantial; under many circumstances it exceeds the contribution by the eddy heat fluxes, $\overline{v'\theta'}$ and $\overline{w'\theta'}$ (cf. pp. 129 and 299 of Andrews *et al.* 1987). This implies that wave-driven heating rates, $\partial\bar{T}/\partial t$, cannot be estimated reliably from calculations of eddy energy fluxes—results obtained in this manner (e.g., French and Gierasch 1974, French *et al.* 1983) should be viewed with caution. Unfortunately, we were unable to characterize the residual mean meridional circulation or to estimate $\partial\bar{T}/\partial t$ given the limitations of the data.

Approximations revisited. Most of the preceding discussion is based on the assumption that wave amplitudes are small enough to justify the neglect of nonlinear effects. We also ignored the possible influence of meridional variations in $\bar{u}$. We now consider the validity of these approximations in light of the results derived so far.

We begin with the small-amplitude approximation. For an inertio-gravity wave propagating in the zonal direction, the condition for stability in Eq. (8) is equivalent to

$$|u'| < |\omega/k - \bar{u}|. \quad (23)$$

When this inequality is violated, the zonal component of fluid velocity, u', is sufficient to cause overturning of surfaces of constant potential temperature, resulting in superadiabatic temperature lapse rates. This condition also shows that wave breaking is inherently nonlinear, since the ratio $|u'|/|\omega/k - \bar{u}|$, a measure of nonlinearity, is of order unity at the breaking level (Walterscheid and Schubert 1990). These considerations suggest that the linear theory should be applied only when the wave amplitude is observed to grow exponentially with height, so that wave breaking has not yet occurred. This appears to be the case for wave 1 (cf. Figs. 8 and 15a). Conversely, the apparent saturation of wave 3 (cf. Figs. 10 and 15b) may be indicative of wave breaking and nonlinear behavior. Results given here for wave 3 should be regarded with extra caution for this reason.

The neglect of meridional wind shear seems justified when:

$$|\partial\bar{u}/\partial y| \ll |f| \quad (24)$$

and

$$|(\partial\bar{u}/\partial y)\delta y| \ll |c|, \quad (25)$$

where δy is the meridional range of the measurements. The first condition follows from the zonal momentum equation, while the second assures that the variation of $\bar{u}$ with latitude produces a negligible Doppler shift in σ_i. We will assess these conditions only for wave 1, since measurements of $\partial\bar{u}/\partial y$ are not available at the latitude of wave 3.

From Fig. 6b of Limaye and Sromovsky (1991), $|\partial\bar{u}/\partial y| \approx 2 \times 10^{-5}\ \text{sec}^{-1}$ at 45°S latitude. Hence, the first condition is satisfied. To evaluate the second condition, we need a value for δy, which we obtained from Fig. 13. At egress, the raypath moved about 300 km in the meridional direction between the 3 and 90 mbar pressure levels, the vertical range of wave 1. Hence, $|(\partial\bar{u}/\partial y)\delta y| \approx 6\ \text{m sec}^{-1}$, comparable in magnitude to the vertically integrated shear between these pressure levels (see above). Comparing this with the constraint on c for wave 1 (>23 m sec^{-1}; Table IV), we conclude that the second condition is also marginally satisfied. Thus, to lowest order, the effect of meridional wind shear can be ignored. This conclusion is somewhat speculative since the wind speeds derived by Limaye and Sromovsky (1991) pertain to the troposphere, whereas wave 1 was observed in the stratosphere. However, the zonal winds appear to decay with height at all latitudes (Conrath *et al.* 1991a) so that estimates of $|\partial\bar{u}/\partial y|$ in the troposphere may be upper bounds on the stratospheric values.

SUMMARY

We conclude with a summary of our principal results (see also Abstract and Tables III–IV):

1. We applied digital filters and techniques of spectral analysis to Voyager 2 radio occultation data, revealing distinct, quasi-periodic temperature variations in the troposphere and stratosphere of Neptune at both 61°N (ingress) and 45°S (egress).
2. Figures 8–11 show measured vertical profiles of the most prominent wave-induced temperature perturbations. The temperature oscillations have ampli-

tudes of 0.1–1 K and vertical wavelengths of 1–10 km.

3. The horizontal wavelength most likely exceeds the vertical wavelength by at least an order of magnitude for each wave observed here. This conclusion follows from numerical simulations of radio occultation measurements and consideration of a condition for atmospheric stability.
4. We confined our interpretation to two waves observed in the stratosphere. Both are probably inertio-gravity waves, since Rossby waves with a vertical structure that matches the observations would have implausibly small zonal phase speeds.
5. The exponential growth of wave amplitude with height should result in wave breaking at pressures less than 0.5 mbars for wave 1 (45°S). Dissipation may already be occurring within the interval of direct observations for wave 3 (61°N).
6. Wave dissipation could produce eddy diffusivities as large as 50 $m^2 sec^{-1}$. Comparisons with independent estimates of this parameter suggest that waves are a significant source of eddy mixing in Neptune's upper stratosphere.
7. The wave forcing of the mean flow that accompanies dissipation could alter the zonal winds by as much as 9 m sec^{-1} per planet rotation. The waves can thereby have a significant influence on the circulation and thermal structure of Neptune's upper stratosphere.
8. The results are seriously limited by our inability to derive tighter constraints on the horizontal structure of the waves.
9. If the apparent saturation of wave 3 is due to dissipation, its horizontal-to-vertical aspect ratio is ~17. The values of $|\sigma_i|$, K_e, and $|\partial\bar{u}/\partial t|$ for wave 3 would then approach the upper bounds given in Table IV, and the value of $|c|$ would be near its stated lower bound.
10. The reliability of our results is constrained by limitations of the standard, linear theory for atmospheric waves. For example, the process of wave dissipation is poorly understood, and estimates of the wave-generated eddy diffusivity are therefore suspect.

ACKNOWLEDGMENTS

This work was made possible through funding from NASA under Grant NAGW-2442 of the Neptune Data Analysis Program. We are indebted to the Voyager Project in general and the Radio Science Team in particular for their efforts in planning and executing the highly successful Neptune flyby.

REFERENCES

ANDERSON, J. D., S. W. ASMAR, J. K. CAMPBELL, R. A. JACOBSON, T. P. KRISHER, E. R. KURSINSKI, E. L. LAU, AND D. D. MORABITO 1992. *Gravitational Parameters for Neptune and Triton.* Presented at Conference on Neptune and Triton, Tucson, AZ, 6–10 January, 1992.

ANDREWS, D. G., J. R. HOLTON, AND C. B. LEOVY 1987. *Middle Atmosphere Dynamics.* Academic Press, Orlando.

BÉZARD, B., P. N. ROMANI, B. J. CONRATH, AND W. C. MAGUIRE 1991. Hydrocarbons in Neptune's stratosphere from Voyager infrared observations. *J. Geophys. Res.* **96,** 18,961–18,975.

BISHOP, J., S. K. ATREYA, P. N. ROMANI, B. R. SANDEL, AND F. HERBERT 1992. Voyager 2 ultraviolet spectrometer solar occultations at Neptune: Constraints on the abundance of methane in the stratosphere. *J. Geophys. Res.* **97,** 11,681–11,694.

BORN, M., AND E. WOLF 1975. *Principles of Optics,* 5th ed. Pergamon, Oxford.

BRACEWELL, R. N. 1986. *The Fourier Transform and Its Applications,* 2nd ed., revised. McGraw–Hill, New York.

BRIGHAM, E. O. 1974. *The Fast Fourier Transform.* Prentice–Hall, Englewood Cliffs, NJ.

CONNERNEY, J. E. P., M. H. ACUÑA, AND N. F. NESS 1991. The magnetic field of Neptune. *J. Geophys. Res.* **96,** 19,023–19,042.

CONRATH, B. J., F. M. FLASAR, AND P. J. GIERASCH 1991a. Thermal structure and dynamics of Neptune's atmosphere from Voyager measurements. *J. Geophys. Res.* **96,** 18,931–18,939.

CONRATH, B. J., D. GAUTIER, G. F. LINDAL, R. E. SAMUELSON, AND W. A. SHAFFER 1991b. The helium abundance of Neptune from Voyager measurements. *J. Geophys. Res.* **96,** 18,907–18,919.

COY, L., AND D. C. FRITTS 1988. Gravity wave heat fluxes: A Lagrangian approach. *J. Atmos. Sci.* **45,** 1770–1780.

ESHLEMAN, V. R. 1973. The radio occultation method for the study of planetary atmospheres. *Planet. Space Sci.* **21,** 1521–1531.

ESHLEMAN, V. R. 1975. Jupiter's atmosphere: Problems and potential of radio occultation. *Science* **189,** 876–878.

ESHLEMAN, V. R., G. L. TYLER, J. D. ANDERSON, G. FJELDBO, G. S. LEVY, G. E. WOOD, AND T. A. CROFT 1977. Radio science investigations with Voyager. *Space Sci. Rev.* **21,** 207–232.

FJELDBO, G., AND V. R. ESHLEMAN 1968. The atmosphere of Mars analyzed by integral inversion of the Mariner IV occultation data. *Planet. Space Sci.* **16,** 1035–1059.

FJELDBO, G., A. J. KLIORE, AND V. R. ESHLEMAN 1971. The neutral atmosphere of Venus as studied with the Mariner V radio occultation experiments. *Astronom. J.* **76,** 123–140.

FLASAR, F. M., AND P. J. GIERASCH 1986. Mesoscale waves as a probe of Jupiter's deep atmosphere. *J. Atmos. Sci.* **43,** 2683–2707.

FRENCH, R. G., J. L. ELLIOT, E. W. DUNHAM, D. A. ALLEN, J. H. ELIAS, J. A. FROGEL, AND W. LILLER 1983. The thermal structure and energy balance of the Uranian upper atmosphere. *Icarus* **53,** 399–414.

FRENCH, R. G., AND P. J. GIERASCH 1974. Waves in the Jovian upper atmosphere. *J. Atmos. Sci.* **31,** 1707–1712.

FRITTS, D. C. 1984. Gravity wave saturation in the middle atmosphere: A review of theory and observations. *Rev. Geophys. Space Phys.* **22,** 275–308.

FRITTS, D. C., AND T. J. DUNKERTON 1985. Fluxes of heat and constituents due to convectively unstable gravity waves. *J. Atmos. Sci.* **42,** 549–556.

GILL, A. E. 1982. *Atmosphere–Ocean Dynamics.* Academic Press, San Diego.

HAMMING, R. W. 1989. *Digital Filters,* 3rd ed. Prentice–Hall, Englewood Cliffs, NJ.

HARRIS, F. J. 1978. On the use of windows for harmonic analysis

with the discrete Fourier transform. *Proc. IEEE* **66,** 51–83.

HINES, C. O. 1970. Eddy diffusion coefficients due to instabilities in internal gravity waves. *J. Geophys. Res.* **75,** 3937–3939.

HINSON, D. P., AND J. A. MAGALHÃES 1991. Equatorial waves in the stratosphere of Uranus. *Icarus* **94,** 64–91.

HODGES, R. R., JR. 1969. Eddy diffusion coefficients due to instabilities in internal gravity waves. *J. Geophys. Res.* **74,** 4087–4090.

HUBBARD, W. B. 1976. Ray propagation in oblate atmospheres. *Icarus* **27,** 387–389.

HUBBARD, W. B., D. M. HUNTEN, AND A. J. KLIORE 1975. Effect of the Jovian oblateness on Pioneer 10/11 radio occultations. *Geophys. Res. Lett.* **2,** 265–268.

INGERSOLL, A. P., C. BARNET, R. F. BEEBE, F. M. FLASAR, D. P. HINSON, S. S. LIMAYE, L. A. SROMOVSKY, AND V. E. SUOMI 1993. Meteorology of Neptune. In *Neptune* (D. Cruikshank, Ed.), in preparation. Univ. of Arizona Press, Tucson.

JENKINS, G. M., AND D. G. WATTS 1968. *Spectral Analysis and Its Applications*. Holden–Day, San Francisco.

KLIORE, A. J., AND P. M. WOICESHYN 1976. Structure of the atmosphere of Jupiter from Pioneer 10 and 11 radio occultation measurements. In *Jupiter* (T. Gehrels, Ed.), pp. 216–237, Univ. of Arizona Press, Tucson.

LEOVY, C. B., A. J. FRIEDSON, AND G. S. ORTON 1991. The quasiquadrennial oscillation of Jupiter's equatorial stratosphere. *Nature* **354,** 380–382.

LIMAYE, S. S., AND L. A. SROMOVSKY 1991. Winds of Neptune: Voyager observations of cloud motions. *J. Geophys. Res.* **96,** 18,941–18,960.

LINDAL, G. F. 1992. The atmosphere of Neptune: An analysis of radio occultation data acquired with Voyager 2. *Astronom. J.* **103,** 967–982.

LINDAL, G. F., J. R. LYONS, D. N. SWEETNAM, V. R. ESHLEMAN, D. P. HINSON, AND G. L. TYLER 1987. The atmosphere of Uranus: Results of radio occultation measurements with Voyager 2. *J. Geophys. Res.* **92,** 14,987–15,001.

LINDAL, G. F., D. N. SWEETNAM, AND V. R. ESHLEMAN 1985. The atmosphere of Saturn: An analysis of the Voyager radio occultation measurements. *Astronom. J.* **90,** 1136–1146.

LINDZEN, R. S. 1981. Turbulence and stress owing to gravity wave and tidal breakdown. *J. Geophys. Res.* **86,** 9707–9714.

LIPA, B., AND G. L. TYLER 1979. Statistical and computational uncertainties in atmospheric profiles from radio occultation: Mariner 10 at Venus. *Icarus* **39,** 192–208.

LOMB, N. R. 1976. Least-squares frequency analysis of unequally spaced data. *Astrophys. Space Sci.* **39,** 447–462.

OPPENHEIM, A. V., AND R. W. SCHAFER 1975. *Digital Signal Processing*. Prentice–Hall, Englewood Cliffs, NJ.

ORCUTT, R. H., AND R. H. COLE 1967. Dielectric constants of imperfect gases. III. Atomic gases, hydrogen, and nitrogen. *J. Chem. Phys.* **46,** 697–702.

PRESS, W. H., AND S. A. TEUKOLSKY 1988. Search algorithm for weak periodic signals in unevenly spaced data. *Computers in Physics* **2**(6), 77–82.

STONE, E. C., AND E. D. MINER 1989. The Voyager 2 encounter with the Neptunian System. *Science* **246,** 1417–1421.

TURNER, J. S. 1973. *Buoyancy Effects in Fluids*. Cambridge Univ. Press, Cambridge.

TYLER, G. L. 1987. Radio propagation experiments in the outer Solar System with Voyager. *Proc. IEEE* **75,** 1404–1431.

TYLER, G. L., D. N. SWEETNAM, J. D. ANDERSON, S. E. BORTUZKI, J. K. CAMPBELL, V. R. ESHLEMAN, D. L. GRESH, E. M. GURROLA, D. P. HINSON, N. KAWASHIMA, E. R. KURSINSKI, G. S. LEVY, G. F. LINDAL, J. R. LYONS, E. A. MAROUF, P. A. ROSEN, R. A. SIMPSON, AND G. E. WOOD 1989. Voyager radio science observations of Neptune and Triton. *Science* **246,** 1466–1473.

WALTERSCHEID, R. L., AND G. SCHUBERT 1990. Nonlinear evolution of an upward propagating gravity wave: Overturning, convection, and turbulence. *J. Atmos. Sci.* **47,** 101–125.

WARWICK, J. W., D. R. EVANS, G. R. PELTZER, R. G. PELTZER, J. H. ROMIG, C. B. SAWYER, A. C. RIDDLE, A. E. SCHWEITZER, M. D. DESCH, M. L. KAISER, W. M. FARRELL, T. D. CARR, I. DE PATER, D. H. STAELIN, S. GULKIS, R. L. POYNTER, A. BOISCHOT, F. GENOVA, Y. LEBLANC, A. LECACHEUX, B. M. PEDERSEN, AND P. ZARKA 1989. Voyager planetary radio astronomy at Neptune. *Science* **246,** 1498–1501.